Citation
Javed, U. and Shaikh, F.U.A. and Sarker, P.K. 2022. Microstructural investigation of lithium slag geopolymer pastes containing silica fume and fly ash as additive chemical modifiers. Cement and Concrete Composites. 134: ARTN 104736. http://doi.org/10.1016/j.cemconcomp.2022.104736

Microstructural investigation of lithium slag geopolymer pastes containing silica fume and fly ash as additive chemical modifiers

Usman Javed, Faiz Uddin Ahmed Shaikh*, Prabir Kumar Sarker

Department of Civil Engineering, School of Civil and Mechanical Engineering, Curtin University, Perth, Australia

***Corresponding author: s.ahmed@curtin.edu.au**

Abstract

Lithium slag is an industrial by-product obtained after lithium extraction from spodumene ore. The higher concentration of sulfate ions (SO_4^{-2}) in the form of gypsum/anhydrite makes it a chemically unviable binder. This research investigates the dilution of the sulphatic component in pore solution by additive incorporation of silica fume and fly ash as chemical modifiers in the lithium slag geopolymer. The setting behavior, detailed microstructural properties, mineral phase quantitative analysis, and compressive strength of lithium slag geopolymer containing fly ash and silica fume were studied. The increasing silica to alumina ratios (Si/Al) by incorporating silica fume in sodium tetraborate added geopolymer resulted in the set retardation after the setting accelerated at Si/Al ratio of 3.5. Similarly, the set retardation was observed for all fly ash replaced lithium slag geopolymers marked by the lower dissolution of SO_4^{-2} ions in pore solution. The fragmented and porous N-(C)-A-S-H gel in lithium slag geopolymer densified by additive incorporation of silica fume and fly ash due to suppressed formation of SO_4^{-2} in pore solution, thus increasing the compressive strength. The main binding zeolite phases quantified in mineral and crystal phase analysis of fly ash replaced geopolymer were mordenite, anorthite, analcime, and calcium chabazite, whereas for silica fume incorporated geopolymer were mordenite, anorthite, analcime, and sodium clinoptilolite. Thus, the lithium slag can be a promising geopolymer precursor along with other supplementary cementitious materials. However, further research is suggested for its chemical viability as a sole geopolymer binder.

Keywords: Lithium slag geopolymer; Fly ash; Silica fume; Sulfates; Rietveld quantitative analysis; Zeolites phases

Abbreviations: SO_4^{-2}, Sulfate ions; Si/Al, Silica to Alumina Ratios; N-(C)-A-S-H, Sodium-Calcium Aluminosilicate hydrate gel; USGS, United States Geological Survey; F^-, Fluorite ions;

DEF, Delayed Ettringite Formation; SEM, Scanning Electron Microscopy; EDS, Energy Dispersive X-ray Spectroscopy; XRD, X-ray Diffraction; XRF, X-ray Fluorescence; $Na_2B_4O_7 \cdot 10H_2O$, Sodium Tetraborate decahydrate; SiO_2/Al_2O_3, Modular Ratio; TIMA, Tescan Integrated Mineral Analyzer; ICDD, International Crystallographic Diffraction Data; ASTM, American Society for Testing Materials; LS-FA, Fly Ash replaced Lithium Slag Geopolymer; LS-SF, Silica Fume added Lithium Slag Geopolymer; Ca/Si, Calcium to Silica Ratios; C-A-S-H, Calcium Aluminosilicate Hydrate Gel; R_{wp}, Weighted Profile R-Factor;

1. Introduction

Lithium slag originated as a waste product after refining spodumene ore to produce lithium hydroxide used in rechargeable batteries, lubricating greases, pharmaceutical, glass, and ceramic industries [1-3]. The lithium demand surge occurred in the late 90s when its use in portable electronic gadgets gained popularity [4]. The recent escalation in the production of electric vehicles has increased the demand for lithium. Approximately 23% rise in lithium production occurred between 2017 and 2018, with values of 69,000 to 85,000 tons [5]. Lithium so far is the only metal used as an electrolyte for high storage and performance of batteries attributed to its excellent energy density (210 $Wh.kg^{-1}$ or 650 $Wh.L^{-1}$) [6], therefore as per the United States Geological Survey (USGS) report, 71% of lithium is used in batteries [7]. It is pertinent to mention that one-ton lithium carbonate production generates approximately 10 tons of lithium slag [8, 9]. Lithium production causes the enormous generation of lithium slag. However, improper dumping might threaten the ecosystem by possibly leaching fluorite (F^-) and SO_4^{2-} [10-12]. Waste disposal of lithium slag has become an environmental concern since its leaching and percolation of the sulphatic component from dumped lithium slag cause serious repercussions to human health.

Lithium is extracted from spodumene, lepidolite, or petalite ore by calcination, followed by acid leaching that produces lithium slag. Spodumene ore is calcined at 1200˚C to enhance its reactivity by converting α to β-spodumene, which subsequently passes through the sulfation process because of the higher stability of lithium sulfate in water [4, 13, 14]. Although lithium slag contains higher silica and alumina content, it is deficient in reactive alumino-silicate phases that might be due to the transformation of aluminosilicate into crystalline polymorphs by calcination [10]. Peltosaari et al. [15] reported that the change of spodumene into tetragonal crystal-shaped β-spodumene polymorph at 1100˚C, and this transformation was initiated at 800˚C.

Since lithium slag is obtained after the sulfation process, it contains a higher concentration of SO_4^{2-} ions in the form of gypsum/anhydrite. Its use as an additive in cement concrete is restricted because of possessing higher SO_3^{2-} ions which might initiate cracks by the excessive generation of ettringite and delayed ettringite formation (DEF) [16, 17]. The sulphatic component also deleteriously affects the development of N-(C)-A-S-H gel in geopolymer

binders. The high sulfate content in lithium slag causes the false setting of geopolymer paste which induces high absorption [8, 18], thus limiting its application as a binder. Few studies have reported the increased reactivity of lithium slag geopolymer by calcination [10] and the addition of sodium tetraborate in the geopolymer matrix [19]. The retardation mechanism of borates was well studied in cement-based binders by Bensted et al. [20], which constitutes a two-step retardation process: (i) Inhibit nucleation of calcium hydroxide; (ii) Encapsulation of cement grains by a protective layer. Another study explained the retardation of calcium sulpho-aluminate cement by the reduced dissolution of aluminate phases and by lowering alkalinity in cement paste matrix [21]. The higher concentration of borates, such as above 7%, significantly retards the setting and severely affects the strength development in high calcium fly ash geopolymer system [22]. However, for low calcium precursors, the borates addition retards the setting of geopolymer, reduces the shrinkage cracking, and results in higher compressive strength. Furthermore, a higher concentration of borates over 5% is detrimental to mechanical strength.

It is an expensive and unsustainable way to change the chemical phase composition of industrial waste for its use as a geopolymer binder. However, the effect of incorporating fly ash and silica fume as chemical additive modifiers in lithium slag is worth investigating for its pragmatic and sustainable disposal solution. Since the lithium slag contains higher proportions of SO_4^{2-} ions, mineralogically in the form of anhydrite (gypsum), this research aims to minimize the deleterious effect of the sulphatic component in lithium slag by separate additive incorporation of fly ash and silica fume to produce geopolymer. This study investigates the initial and final setting behavior, mechanical strength, microstructural investigation of lithium slag geopolymer containing varying replacement proportions of fly ash and increasing silica to alumina ratio by enhancing silica fume in separate mixes. The microstructural analysis includes Scanning Electron Microscopy (SEM) and Energy Dispersive Spectroscopy (EDS) for identifying alkali-aluminosilicate gel morphology and chemical composition. X-ray diffraction (XRD) and Rietveld refinement were employed to identify and quantify the amorphous content and crystallographic mineral phase identification in geopolymer pastes.

2. Materials and Methods

2.1. Raw Materials

The primary precursor was lithium slag which was used after calcining at 700°C, whereas the chemical modifiers in geopolymer were silica fume and fly ash. Commercially supplied amorphous and densified silica fume (specific area of 15-30 m^2/kg) was used, which was provided by Ecotec [23]. Sodium tetraborate (borax) was used to retard the abrupt setting of silica fume added geopolymer. The chemical oxide compositions of lithium slag, silica fume, and fly ash are shown in Table 1. Powdered borax containing 99% concentrated sodium tetraborate decahydrate ($Na_2B_4O_7 \cdot 10H_2O$) was used. Sodium hydroxide and sodium silicate were used as alkaline activators supplied by Rowe Scientific and PQ Australia, respectively. The concentration of sodium hydroxide solution was eight molars, whereas sodium silicate (specific gravity 1.53 g/cm^3) was composed of Na_2O, SiO_2, and water content of 14.70, 29.40, and 55.90%, respectively.

2.2. Characterization

The particle size distribution, micromorphology, chemical, crystallographic, and mineral phase compositions of calcined lithium slag were studied by conducting laser-diffraction particle size distribution analysis, SEM/EDS, XRF, XRD, and Tescan Integrated Mineral Analysis (TIMA), respectively.

The particle size distribution of lithium slag was determined using a Malvern Panalytical Mastersizer 2000 based on the laser diffraction method based on Mie's theory of light scattering [24]. The particle size was determined in ethanol suspended lithium slag particles, the laser-diffraction pattern of the incident laser beam was collected on a laser diffractometer, and the particle size distribution was achieved. The powdered specimens of lithium slag and sodium tetraborate decahydrate were placed on carbon tapped stub followed by sputter coating of carbon which was subsequently tested for SEM/EDS on Tescan VEGA 3. The quantitative oxide composition of calcined lithium slag was determined to be spiked with 4% lithium nitrate as an internal standard. The mixture was first melted into glass beads using Spectromelt-MERCK® flux containing 66 to 34 di-lithium tetraborate and Lithium metaborate. However, the loss on ignition was performed using a robotic arm-based thermogravimetric analyzer between 110 to 1000°C. The XRD of powdered lithium slag specimen was performed upon mixing 10% weight of fluorite as an internal standard,

micronized in ethanol suspension for 10 minutes to get the homogenous mixture. The specimen was dried for 24 hours on a hotplate (40˚C) and was filled in the specimen holder step by step with a glass slide to avoid the preferred orientation of crystals [25]. Mineral phase identification analysis on resin impregnated polished geopolymer pastes and lithium slag specimens were conducted using a Tescan Integrated Mineral Analyzer (TIMA). The resin-impregnated specimens were ground up to a grain size of 9 μm to achieve a polished surface with a maximum irregularity of 1 μm. Sample preparation protocols were adopted from previous research [26]. An 8×8 mm^2 representative area of geopolymer specimens was selected for the detailed scan resulting in a backscattered micrograph, mineral phase maps, and EDS spectral micrographs selecting the pixel size of 1 μm.

The laser particle distribution results in Figure 1 show that the lithium slag contains a wide range of particle distribution between 280 nm to 470 μm with an average particle size of 43.15 μm. The lower slope of the frequency distribution curve on the finer side indicates a higher proportion of finer particles below 70 μm. The discontinuity on the top of the frequency distribution curve indicates particles clustering due to the zeta-potential on the powder surface [27]. The lithium slag is composed of angular particles rich in alumino-silicate minerals; however, the prismatic/elongated particles are composed of gypsum, which is evident in SEM/EDS as shown in Figure 1-a. The EDS points B and C on the micrograph represents the peaks of aluminum, silicon, and oxygen EDS spectra, indicating the aluminosilicate particles. The EDS of prismatic particles revealed the spiked intensity of calcium, sulfur, and oxygen, indicating the presence of gypsum, which provides evidence of sulphation upon lithium extraction in refineries [28]. The prismatic particles are sized over 50 μm.

Along with the calcination of lithium slag, the aluminosilicate turned into agglomerated amorphous (glassy) phase by sintering aluminosilicates. The fragmentation of particles occurred during the lithium refining process of spodumene ore which induces slight reactivity in lithium slag. As the crystalline phase transformation in lithium slag starts from 800˚C onward [15], 700˚C is a suitable temperature for producing amorphous aluminosilicates [10]. The Rietveld refinement results (Figure 3) revealed that the lithium slag contains 84% of amorphous content along with calcite, muscovite, anhydrite/gypsum, albite, anorthite, quartz,

and spodumene content of 5.68, 3.90, 1.50, 1.00, 2.00, 1.04, and 0.93% respectively. The goodness of fit and weighted R-factor values of the Rietveld refinement were 1.14 and 7.78%, indicating the better model alignment of crystallographic phases with observed peaks. It is pertinent to compare the results of Rietveld refinement with XRF and laser particle size distribution. It is interpreted from the characterization results that the lower size fraction of micro and nano-sized is mainly composed of amorphous aluminosilicates. The primary mineral phases were spodumene, anorthite, quartz, and calcite, with 62.25, 9.79, 4.87, and 3.56%, respectively. The quantified mineral phases mapped in EDS spectral phase map presented in Figure 4 are aligned with those reported in the published literature [29]. Spodumene and anorthite are the primary aluminosilicate sources shown in Figure 4, which would participate in polycondensation and the formation of alkali-aluminosilicate gel [30, 31]. The higher difference between mineral and crystal phases is due to the polycrystalline nature and crystal defects in the lithium slag [29]. It is evident from the literature [32-37] that the concentration of the glassy phase imparts the reactivity to the precursor. Hence, the prismatic/elongated particles are primarily composed of anhydrite with a particle size over 50 µm. It is pertinent to mention that the excessive sulfate content in the binder might have a destructive effect on the hydration phases of the binder [16]. Therefore, the anhydrite/gypsum in lithium slag must be chemically suppressed for its use as a geopolymer precursor.

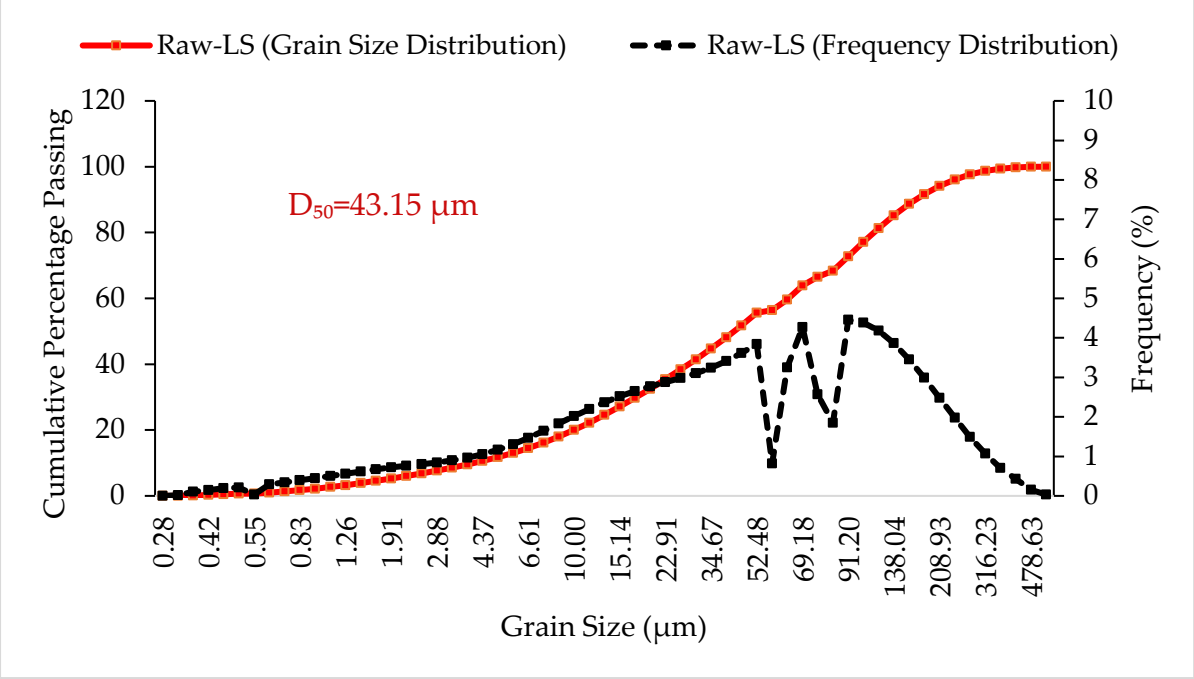

Figure 1: Grain size distribution and frequency distribution of lithium slag [26]

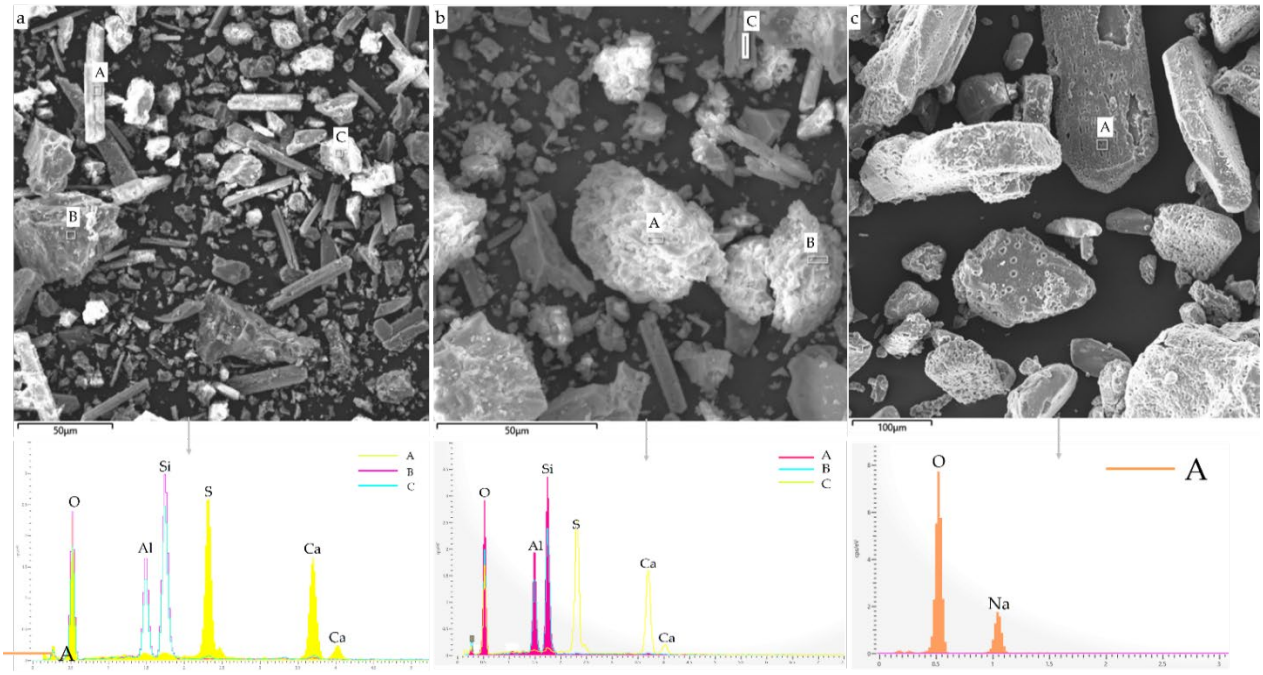

Figure 2: a) Raw lithium slag b) Calcined lithium slag c) Sodium Tetraborate

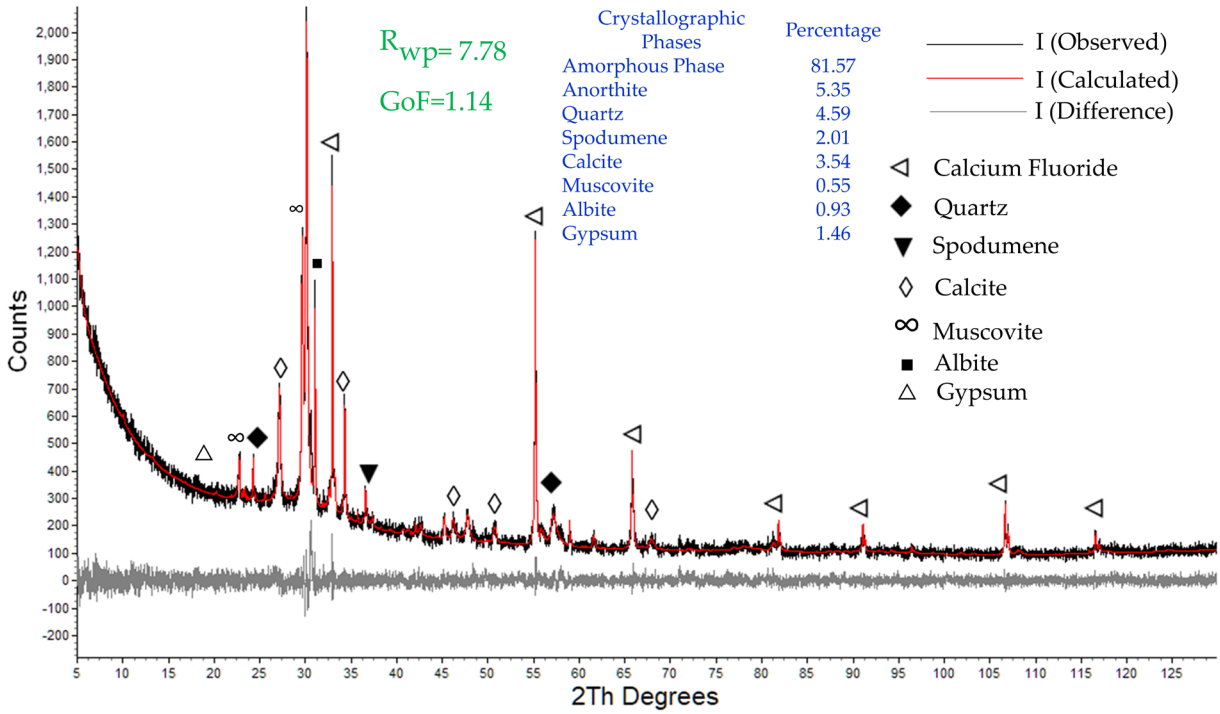

Figure 3: X-ray Diffraction plot and Rietveld refinement of calcined lithium slag (Note: Peaks of Calcium Fluoride indicate the added control sample)

Phases	Conc.(%)
Spodumene	62.25
Unidentified Phase	13.72
Anorthite	9.79
Quartz	4.87
Calcite	3.56
Plagioclase	0.93
Muscovite	1.38
Albite	1.13
Cumulative of Calcium Sulphate, Orthoclase, Actinolite, Dolomite, Hematite, Garnet	2.13
Traces	0.24

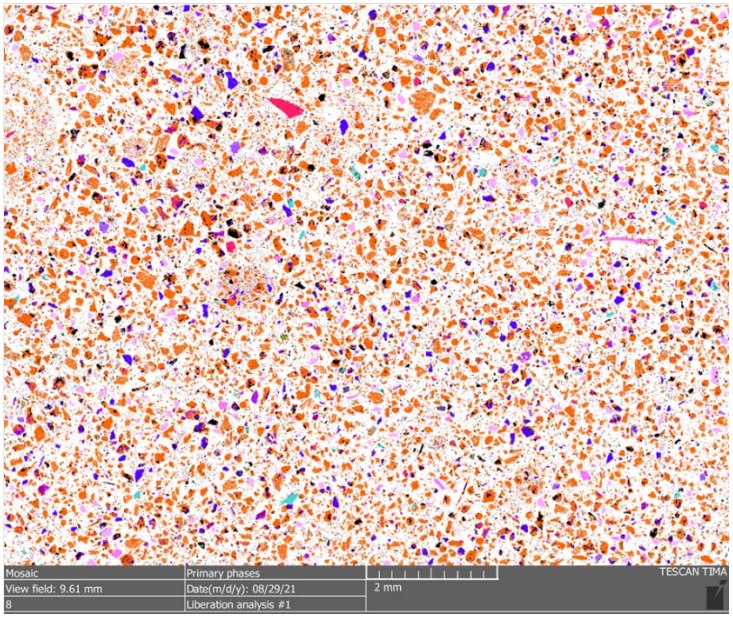

Figure 4: Phase micrograph of lithium slag calcined at 700˚C

Table 1: Chemical composition of calcined lithium slag, silica fume, and fly ash

Oxides	SiO_2	Al_2O_3	Fe_2O_3	CaO	MgO	MnO	TiO_2	SO_3	P_2O_5	K_2O	Na_2O	LOI
Lithium slag [26]	54.53	21.08	1.45	7.53	0.57	0.23	0.05	5.62	0.48	0.88	0.72	6.76
Silica Fume [23]	94.58	0.50	0.06	1.54	0.41	-	-	0.14	0.11	0.64	0.23	1.79
Fly ash [38]	55.90	26.94	6.59	4.25	1.51	0.10	1.43	0.20	0.50	0.76	0.31	1.51

2.3. Mix Proportions

The lithium slag geopolymer pastes containing 0, 25, 50, 75, and 100% replacement of fly ash were produced. The effect of enhancing silica to alumina ratios such as 2.5, 3.5, 4.5, and 5.5 using additive silica fume in lithium slag geopolymer was also investigated. To avoid a false setting, sodium tetraborate was mixed within a silica fume-based lithium slag geopolymer as a retarder [19]. The alkaline activator contains a sodium silicate to sodium hydroxide ratio of 3, and constant water to binder ratio of 0.40 was selected, as shown in Table 2a & b. Aside from the water content present within activators, surplus water was added to fly ash, and silica-fume-based lithium slag geopolymer mixes to achieve the desired consistency of lithium slag pastes.

Consequently, the modular ratio (SiO_2/Al_2O_3) of 1.16 was selected to achieve high compressive strength as reported in the literature [19, 39]. The alkaline activator contains 75% sodium

silicate, 25% sodium hydroxide, and a water content of 40% so that the alkalinity of the pore solution reaches a pH value over 12.5 [40]. The ratios of alkalis to alumina, water to alumina, and silica to sodium oxides remained fixed for lithium slag-fly ash (LS-FA) geopolymer mixes and the silica variations to alumina ratios are attributed to the higher concentration of alumina in fly ash. However, the silica to alumina ratio increased upon incorporating silica fume in lithium slag geopolymer pastes.

Table 2-a: Mix proportioning of LS-FA geopolymer mixes

Abbreviations	Lithium Slag (kg/m^3)	Fly ash (kg/m^3)	Added Water (kg/m^3)	Sodium Hydroxide (kg/m^3)	Sodium Silicate (kg/m^3)	M_2O/Al_2O_3	SiO_2/Al_2O_3
100LS0FA	1212	0	232	106	318	0.46	3.11
75LS25FA	909	303	232	106	318	0.41	2.97
50LS50FA	606	606	232	106	318	0.37	2.84
25LS75FA	303	909	232	106	318	0.33	2.72
0LS100FA	0	1212	232	106	318	0.29	2.61

Note: Ms=$Na_2SiO_3/NaOH$=3, H_2O/Al_2O_3 =0.51, SiO_2/NaO_2 =1.16, Molarity of NaOH=8, W/B=0.40, M_2O: Alkali oxides, Si/Al: Silica to alumina ratios of precursor

Table 2-b: Mix proportions of lithium slag geopolymer at varying Si/Al ratios along with 3% added borax

Abbreviations	Lithium Slag (kg/m^3)	Silica Fume (kg/m^3)	Added water (kg/m^3)	Si/Al	Sodium Hydroxide (kg/m^3)	Sodium Silicate (kg/m^3)	M_2O/Al_2O_3	SiO_2/Al_2O_3
100LS0SF	1202	0	230	2.5	106	318	0.46	2.50
80LS20SF	971	231	230	3.5	106	318	0.48	3.50
70LS30SF	844	359	230	4.5	106	318	0.50	4.50
60LS40SF	730	472	230	5.5	106	318	0.52	5.50

Note: Borax=3%, Ms=$Na_2SiO_3/NaOH$=3, H_2O/Al_2O_3 =0.02, SiO_2/NaO_2 =1.16, Molarity of NaOH=8, W/B=0.40

2.4. **Preparation of Geopolymer**

The geopolymer pastes were produced by mixing lithium slag with mineral additives, activator solution, and water in a Hobart mixer for one-and-half minutes. Initially, the mixer

containing the precursors was run at 116 rpm for thirty seconds for dry mixing, followed by wet mixing with added water and alkaline activators at 380 rpm for the rest of the mixing time. Lithium slag-based geopolymer paste was poured into oiled acrylic cubes of size 50x50x50 mm^3. After that, the geopolymer paste was compacted on a vibrating table for one minute. For the accelerated curing regime, cube molds containing fresh paste were wrapped in polyethylene sheet to avoid moisture loss from the surface and placed in an oven at 70˚C for 24 hours. Then, the hardened specimens were unmoulded and kept at 25˚C and 55% relative humidity till the testing age. Geopolymer cubes were kept at 25˚C and 55% relative humidity afterward until the testing ag.

2.5. Testing Program

Microstructural investigation of lithium slag geopolymer was performed by SEM/EDS, percentage void analysis, XRD, and Rietveld quantitative analysis. Lithium slag-based geopolymer was tested for initial, final setting time, and compressive strength.

2.5.1. SEM/EDS and surface porosity

SEM/EDS was conducted on the carbon-coated geopolymer paste specimens using secondary electron, backscattering electron, and EDS detectors of SEM Tescan Vega 3 to identify and characterize the geopolymer paste matrix and to investigate the microstructural morphology of geopolymer paste. The 10x10 mm^2 rectangular specimens were extracted using a ceramic saw. The specimens were coated with a carbon coating of approximately 20 nm thickness in the Cressington (Model 208HR) sputter coater after attaching to stubs with carbon tape. Moreover, the SEM micrographs and EDS spectra were taken at 10 and 15 kV, respectively. The SEM/EDS analysis manifested a qualitative analysis based on the relative abundance of elements to identify and characterize the aluminosilicate gel in the geopolymer paste matrix based on Ca/Si and Si/Al ratios. Similarly, the identification of microstructural morphology using EDS spectra on unpolished specimens is also suggested by numerous published studies [41-48]. Moreover, the percentage void area was drawn using Image-J software and SEM micrographs as input images.

2.5.2. XRD and Rietveld quantitative analysis

The quantitative Rietveld analysis was performed on a powdered lithium geopolymer sample containing 10% of calcium fluoride as an internal standard for identifying amorphous phases in geopolymer, small internal standard such as 10% provides high accuracy of Rietveld refinement [49]. The chunk of the geopolymer sample was extracted, and the chunks were ground in a ring mill, followed by adding 10% weight of calcium fluoride. Afterward, the mixture was micronized in the ethanol suspension for ten minutes and dried at 40° C on a hotplate for 24 hours. The residual powder was filled in a sample holder and used for a diffraction scan. XRD was performed using Bruker D8 Advance Bragg-Brentano Diffractometer with the Cobalt (Co Kα, λ=1.789 Å) as a radiation source and coupled with LynxEye X-ray detector. The operating conditions were 35kV and 40 mA of voltage and current, respectively. The diffractogram data was recorded between a 2θ scan of 5-130° and a step size of 0.013°. The peak phase identification of spiked geopolymer pastes powdered specimens was performed using DIFFRAC EVA software coupled with International Crystallographic Diffraction Data (ICDD, PDF-2 release 2019). The Rietveld quantitative analysis was performed on Topas software (Bruker AXS version 5). The parameters adopted for Rietveld refinement are as follows in Table 3.

Table 3: Parameters for XRD Rietveld quantitative analysis in Topas Bruker AXS v.5 [26]

Instrument		**Bruker D8 Advance (Automated)**
Radiation Source		Co_Kα (λ=1.789Å, 35kV, 40 mA)
Geniometry range		5-130°
Step Size		0.013°
Counting Time		0.7 sec
Rietveld Refinement		**TOPAS (Bruker AXS Version 5)**
Primary and Secondary radius		217 mm
Equatorial Convolution	Angular range	3.384°
	FDS angle	0.3°
Axial Convolution	Source length	12 mm
	Primary and secondary Soller	2.3°

2.5.3. Setting time

The initial and final setting times were tested by a Vicat apparatus at a temperature of 25°C. The diameter of the needle was 1 mm, and the adopted test procedure complied with ASTM C191-13 [50].

2.5.4. Compressive strength

Geopolymer paste specimens were tested for compressive strength on Shimadzu 300 kN universal testing machine at the age of testing along with the loading rate of 0.24 MPa/sec, complying with the standard test method of ASTM C109 [51].

3. Results and discussion

3.1. The setting of LS-FA geopolymer

The initial and final setting time of lithium slag with increasing replacement of fly ash is shown in Figure 5. The results revealed that the control lithium slag geopolymer has as low as 2.50 and 5.33 minutes of initial and final setting times, respectively. However, the increasing replacement of lithium slag with fly ash increased the initial and final setting time. The geopolymers' initial and final setting time with 25, 50, 75, and 100% replacement of lithium slag by fly ash was recorded as 5.86, 18.91, 118, 192, and 12.05, 38.08, 225, and 356 minutes, respectively. The abrupt setting of lithium slag geopolymer was caused due to false setting attributed to the presence of over 5% of SO_4^{2-} ions in the form of gypsum/anhydrite in lithium slag. As the dissolution of needle-like gypsum in lithium slag increased upon the addition of alkaline activators, the pore solution became highly saturated with SO_4^{2-} and the secondary gypsum precipitated. Sudden stiffening of geopolymer paste is linked with the precipitation of interlocked needle-shaped gypsum (anhydrite) [52], which also causes self-desiccation of geopolymer paste matrix due to the reduction of water content in aluminosilicate gel [16, 53-55]. The EDS spectral micrographs containing mapped spectra of Ca, S, and Si of the regular lithium slag geopolymer (100LS0FA) are shown in Figure 6-a. The similar distribution pattern of calcium and sulfur spectra on the microstructure indicates that the calcium sulfate imparted impurity to aluminosilicate gel. The calcium sulfate in aluminosilicate gel has attributed porosity and caused cracking that might be initiated due to self-desiccation, which can be seen in the BSE micrograph in Figure 6-a. Aside from the calcium sulfate dissolution in

aluminosilicate gel, the EDS spectral mapping of the detected calcium and sulfur spectral data in the bright region indicates the crystalline formation of needle-shaped sodium sulfate as presented in Figure 6-b. This needle-shaped microstructure was produced after alkali activation of anhydrite particles which may have contributed to the loss of the setting of geopolymer paste. Therefore, sulphatic component exists in the form of calcium and sodium sulfate, which was diluted in the geopolymer paste solution that retards the false setting by replacing lithium slag with fly ash. That's why at higher replacement of lithium slag by fly ash, the effect of gypsum diminishes significantly at 50 and 75% fly ash content, marked by higher setting times. Therefore, the higher concentration of SO_4^{2-} in geopolymer paste causes an abrupt setting, similar to cement-based material.

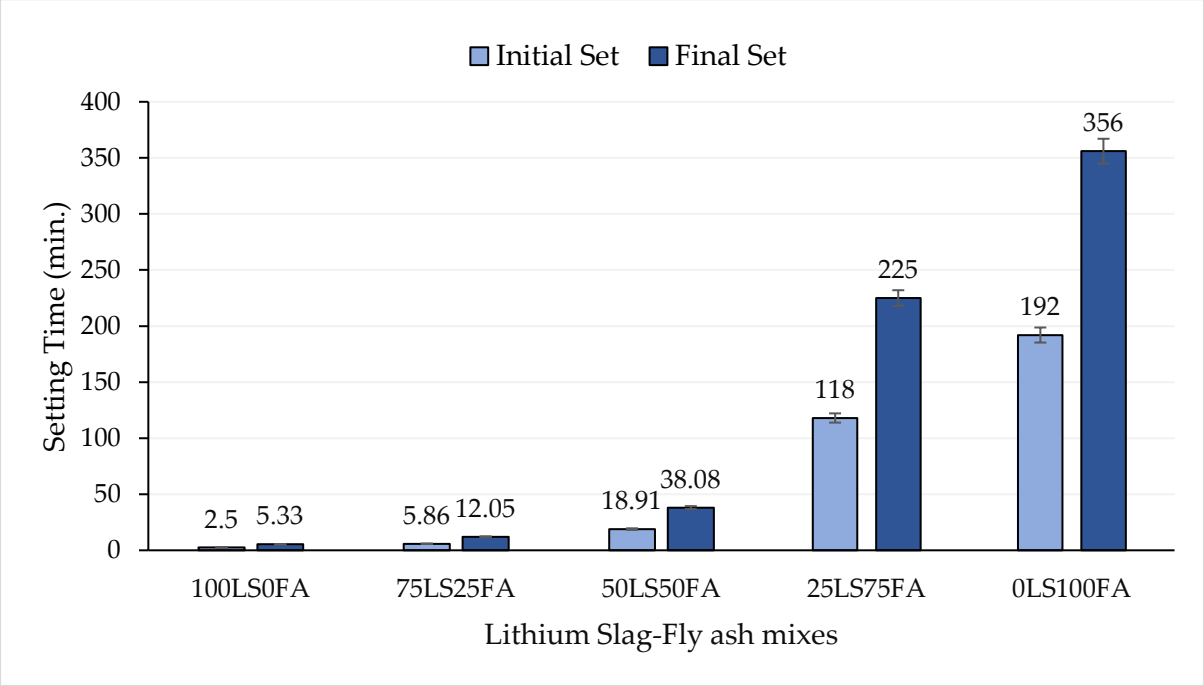

Figure 5: Setting time of lithium slag geopolymer at varying proportions of fly ash replacements

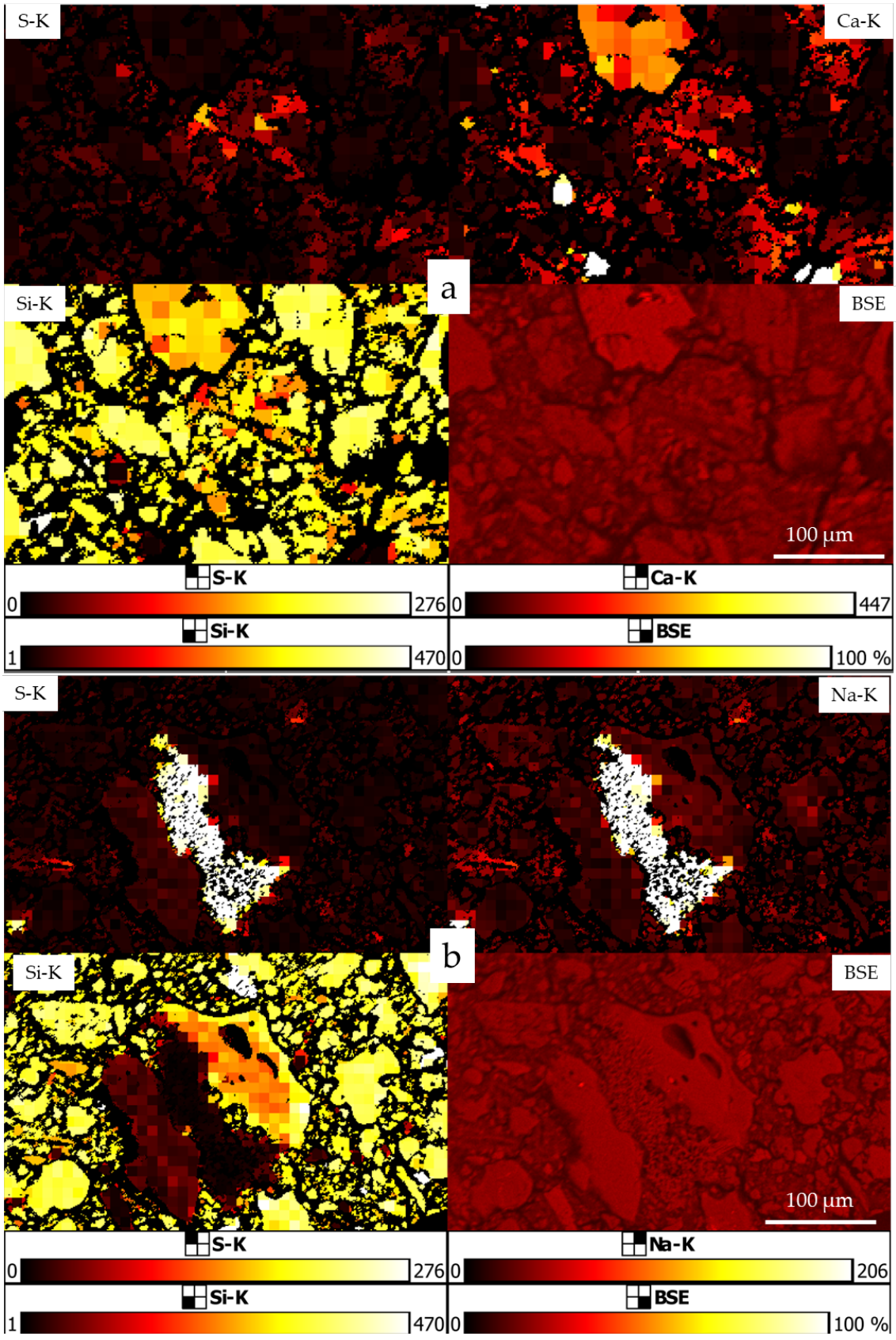

Figure 6: Spectrally mapped EDS micrographs of 100LS0FA mix a) Calcium sulfate distribution in aluminosilicate gel microstructure b) Crystalline sodium sulfate formation after alkali activation

3.2. Setting behavior of LS-SF geopolymer

The setting time of lithium slag added silica fume (LS-SF) geopolymer paste at various Si/Al ratios is presented in Figure 7. As per the higher reactivity of added silica fume and the anticipated abrupt setting of lithium slag geopolymer paste, the incorporated 3% of sodium tetraborate in geopolymer paste retarded its setting, which was previously investigated by Wang et al. [19]. The set retardation in the control lithium slag geopolymer and a Si/Al ratio of 2.5 was observed with the incorporation of sodium tetraborate. Therefore, the initial and final setting time was retarded from 2.5 and 5.33 min to 13.07 and 20.38 min, respectively. The initial and final setting times of geopolymer mixes at Si/Al ratios of 2.5, 3.5, 4.5, and 5.5 were 13.07, 11.83, 14.23, 15.50 min, and 20.38, 19.17, 22.50, 24.7 min, respectively. The initial and final setting time of geopolymer mixes increased 20.28% and 17.37%, and 8.92% and 9.77% from Si/Al values of 3.5 to 4.5 and 4.5 to 5.5, respectively. The maximum increase of initial setting time over 20% indicated the highest suppression of formation of secondary anhydrite at a Si/Al ratio of 3.5. Unlike cement-based material, the literature suggests that the setting of high calcium geopolymer depends on the dissolution of C-A-S-H gel instead of AFt in pore solution [19-21]. Also, precipitation of borate-based phases has not occurred. Instead, boron species were chemically bonded with the aluminosilicate oligomers [19]. The effect of increasing the Si/Al ratio on fly ash-based geopolymer was studied in the literature [56], and it was reported that the setting time decreased at a Si/Al ratio of around 4. However, for LS-SF geopolymer, the setting accelerates at a Si/Al ratio of 3.5, which decelerates subsequently upon increasing Si/Al ratios. Hence, the incorporation of fly ash and silica fume in lithium slag geopolymer retarded its setting.

Wang et al. [19] investigated the reaction mechanism of sodium tetraborate in lithium slag geopolymer. The retardation mechanism of sodium tetraborate containing geopolymer is quite different from the cement-based material in that the borate (BO_3) delays forming Si-O-Al bonds. From MAS-NMR spectroscopy, the borate group was identified in the form of Trigonal [BO_3] and tetrahedral [BO_4] structure which is indicated as $^{[3]}B$ and $^{[4]}B$, respectively [19]. The added borate first reacts with the silicate group to form B-O-Si bonding in the presence of low alkalinity, followed by $^{[4]}B$-O-Si bond breakage by aluminate tetrahedron $[AlO4]^-$ and subsequent formation of $^{[3]}B$-O-Al-O-Si. $^{[3]}B$ has much higher bond energy than

[4]B indicating more stability of [3]B-O-Al-O-Si compound. Moreover, the formation of [3]B-O-Al-O-Si reduces the reaction rate, thus retarding the setting time of LS-SF geopolymer.

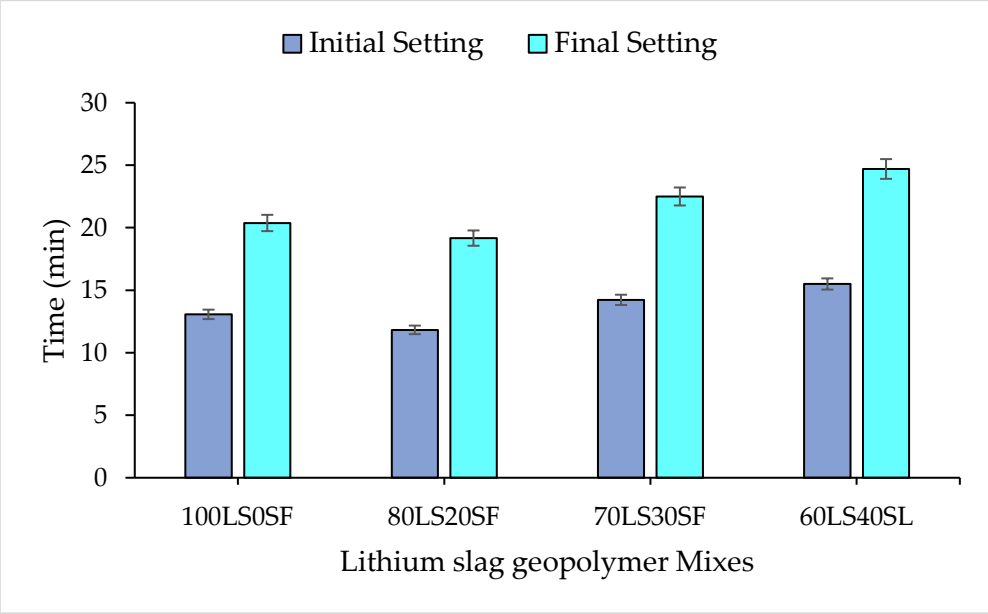

Figure 7: Setting time of lithium slag geopolymer at varying silica to alumina ratios

3.3. Effect of borax on geopolymer chemistry

The addition of borax has resulted in the stability of the geopolymer paste matrix in terms of better mechanical strength. The geopolymer paste microstructure is chemically assessed based on EDS data points on SEM micrographs. Figure 8 compares the chemical composition and morphology of lithium slag geopolymer pastes with and without sodium tetraborate addition. The chemical composition of C-(N)-A-S-H gel varied with sodium tetraborate addition in lithium slag geopolymer. The point EDS and small area EDS of unpolished specimens can produce EDS spectra that might be used for qualitative purposes, such as identification of microstructural morphology based on Si/Al ratios as suggested by various studies [42, 45, 46, 48]. The qualitative relative abundance of elements to identify and characterize the N-(C)-A-S-H gel is evident in the literature [41-48]. The alkali activation of lithium slag geopolymer precipitated the fragmented C-(N)-A-S-H gel (Figure 8-b) containing microcracks, whereas the addition of sodium tetraborate produced densified microstructure with fewer cracks, representing N-(K)-A-S-H gel as per EDS analysis (Figure 8-d). The EDS results indicated that the control lithium slag geopolymer contains a higher concentration (EDS B) of dissolved Sulfate ions (SO_4^{-2}) in C-A-S-H gel, suspected of causing its self-desiccation. The crack formation indicates the self-desiccation of geopolymer paste by the

appearance of secondary gypsum in the form of anhydrite and its saturation in pore solution upon polycondensation of alumino-silicate polymorphs causes the consumption of water content. Li and Fall [16] investigated the effect of sulfate on the shrinkage of cementitious paste in which sulfate ions react with tricalcium aluminate producing ettringite, and sulfates dissolution in calcium silicate hydrate gel causes the disintegration in the microstructure. Thus, the self-desiccation phenomenon is common both in cement hydration and geopolymerization due to excess gypsum content in pore solution.

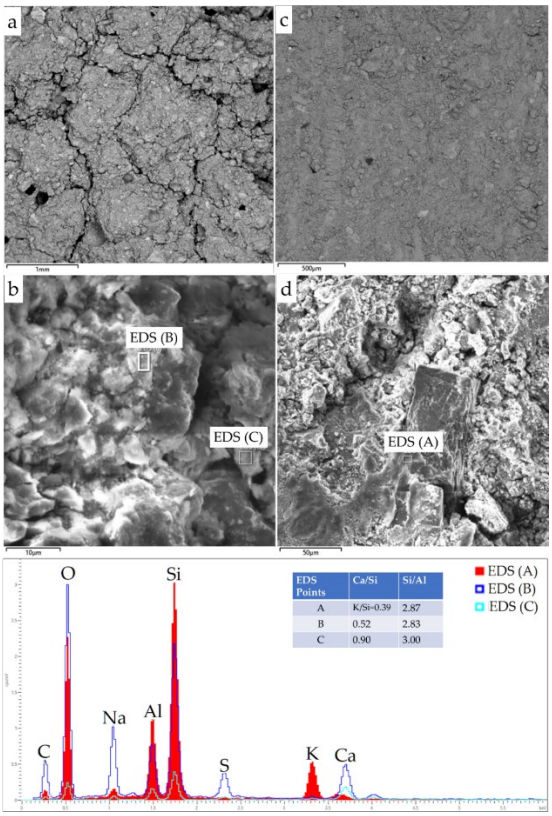

Figure 8: SEM micrographs of lithium slag geopolymer paste (a,b) and borax added lithium slag geopolymer paste (c, d)

3.4. Void percentage

The percentage voids of lithium slag geopolymer containing fly ash are shown in electron micrographs in Figure 9. Micrographs depicting the dark void area show the processed SEM images in open-source Image-J software. Interconnected microcracks have been observed in the control lithium slag geopolymer, which is extended throughout the microstructure, as shown in Figure 9a.

The lower magnification of SEM micrographs was selected to determine the void ratio so that uneven grain undulation of a few microns could not significantly affect the accuracy of the void analysis. Therefore, cracks and voids appeared in 100% lithium slag geopolymer paste even at lower magnification, indicating higher porosity. The percentage void area for 100LS0FA, 50LS50FA, and 0LS100FA mixes were 7.29, 4.76, and 1.20%, respectively. The crack formation decreased due to incorporating 50% fly ash in lithium slag geopolymer attributed to dilution of sulfates in pore solution and reduced cracking. Therefore, the porosity is associated with sulfate ions in geopolymer paste. The discontinuation of cracks and formation of fewer voids were observed in the geopolymer paste surface with a percentage void area of 4.76% comparative to the control lithium slag geopolymer (7.29%). The void area was further reduced to 1.20% for regular fly ash-based geopolymer paste. Hence, over 34% reduction in voids upon replacing lithium slag with 50% fly ash occurred. Literature suggested that the surface porosity of cement paste matrix containing ferronickel slag resulted in similar trends of surface porosity as compliant with the bulk percentage porosity [57]. Another research determined the uniformly distributed foam bubbles on the surface of foam concrete containing bagasse ash as supplementary cementitious material by image analysis using MATLAB code. The percentage voids specified from image analysis of macro pores followed the micropores determined in SEM analysis [58]. Although the determination of porosity by image analysis only corresponds to the surface porosity that can be correlated with the lithium slag geopolymer composite's bulk porosity, detailed investigations are included in the plan for future research.

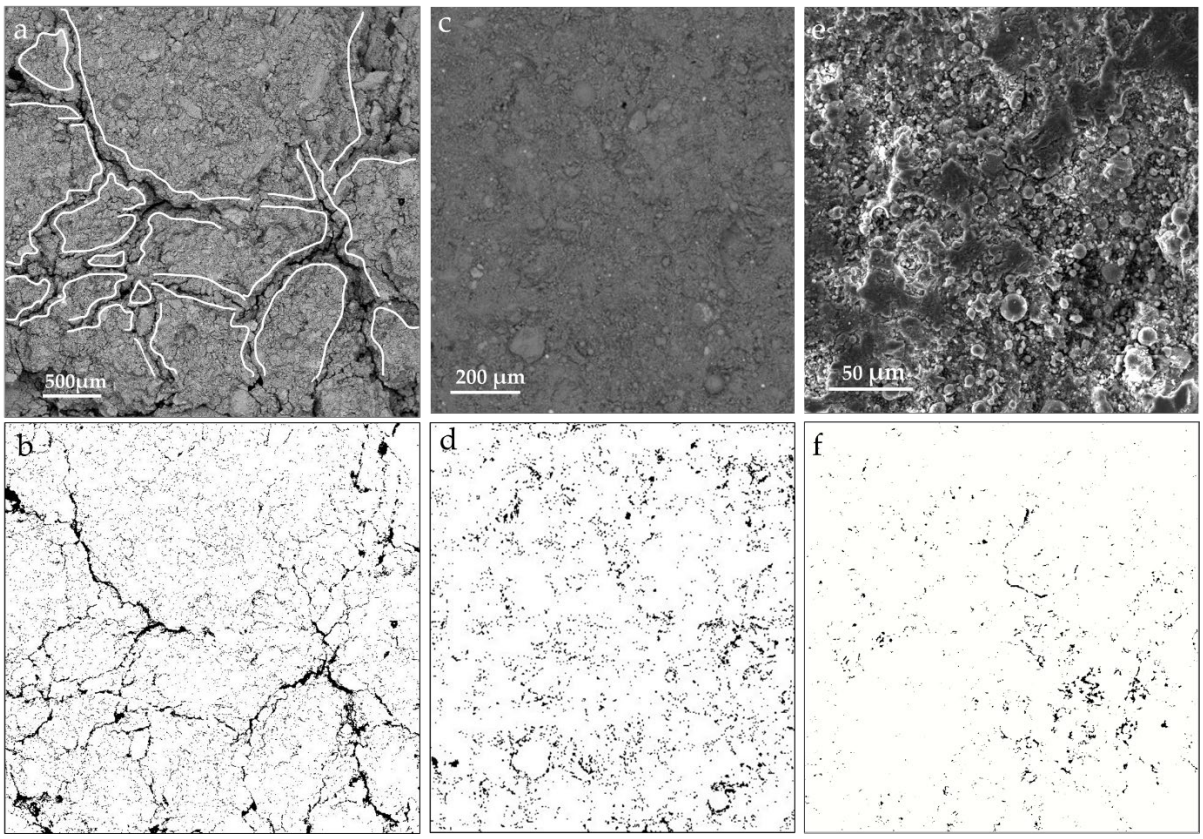

Figure 9: Calculation of void area from SEM micrographs of LS-FA geopolymer specimens (a, b: 100LS0FA; c, d: 50LS50FA; e, f: 0LS100FA)

Table 4: Percentage voids in lithium slag geopolymer

	Total Area (μm^2)	Void Area (μm^2)	Percentage Void ($\mu m/ \mu m$)
100LS0FA	13,834,800	1,008,556	7.29
50LS50FA	3,690,682	175,676	4.76
0LS100FA	53,356	640	1.20

3.5. Microstructural investigation of lithium slag geopolymer

3.5.1. Phase characterization of aluminosilicate gel

The low calcium alkali activated system such as lithium slag geopolymer contains complex geo-chemistry with highly crosslinked polysilicate (-Si-O-Al-) tetrahedral structure. The aluminosilicate gel (N-(C)-A-S-H) was characterized using automated SEM/EDS on resin-impregnated polished geopolymer specimens are shown in Figure 10. Mordenite and anorthite phases were generated in hydrothermal conditions while curing at 70° C [59], which were identified as a zeolitic component of the alkali aluminosilicate gel system. The polycondensation of aluminosilicates from leached spodumene and association of

alkali/metal cations at tetrahedral Al sites yielded a mordenite zeolite phase (24.08%) as a primary alkali-aluminosilicate gel.

In the 100LS0FA geopolymer paste specimen, albite formation was prominent after geopolymerization, which drastically increased from 1.13% in lithium slag to 48.24% in lithium slag geopolymer mix (Figure 10-a). The microstructure of the 100LS0FA mix contains wider cracks and voids among all the mixtures. The crack width and the entrapped air bubble ranged between 10-50 microns and 75-150 microns, respectively. The presence of wider cracks and voids is apparently due to inadequate N-(C)-A-S-H gel for encapsulating the lithium slag particles. The aluminosilicate gel spiked in 50% fly ash replaced lithium slag geopolymer, which was attributed to the generation of 53.17% mordenite phase. It is pertinent to mention that the molecular and crystal structure of zeolites and alkali aluminosilicate gel resembles each other, which has been studied by Davidovits [60], Glukhovsky [61], and in various other published studies [62-65]. The inclusion of fly ash with lithium slag geopolymer resulted in the higher mordenite phase that densified the microstructure by encapsulating the precursor particles. However, the anorthite phase in fly ash replaced geopolymer bounded the microstructure within the voids of precursor particles, thus resulting in a densified microstructure (Figure 10-b, f).

In silica fume replaced lithium slag geopolymer (100LS0SF), the anorthite phase increased to 22.10%, compared to 15.81% in 100LS0FA. The increase is attributed to the addition of sodium tetraborate. Sodium tetraborate addition in lithium slag does not precipitate a new crystal phase [19]. However, it increased the dissolution of aluminosilicates and reduced voids and cracks, which can be seen in Figure 10-a, c. The phase micrograph of the silica fume rich mix (60LS40SF) depicted a higher concentration of silica in the form of quartz. The mineral phases such as albite, mordenite, quartz, and anorthite increased significantly to 36.16, 29.21, 16.11, and 10.28%, respectively. The higher rate of polycondensation of aluminosilicate at the juncture of silica-rich quartz particles has caused the local cracks within silica particles that might have originated due to the self-desiccation of alkali-aluminosilicate gel. Hence, substituting fly ash and silica fume has improved the geopolymer microstructure by generating higher alkali aluminosilicate gel.

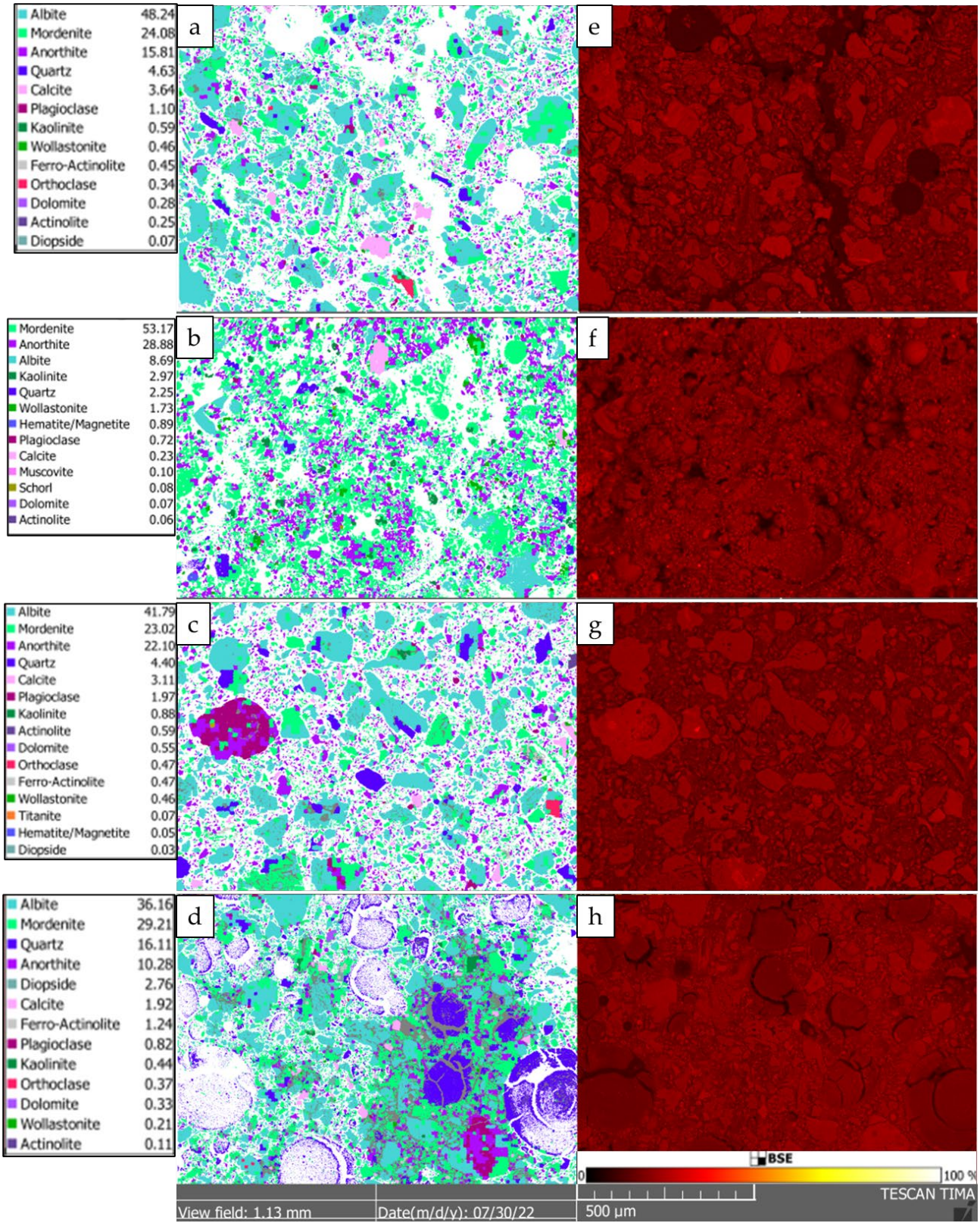

Figure 10: Mineral phase micrograph and corresponding backscattered micrograph of geopolymer pastes, a, e: 100LS0FA; b, f: 50LS50FA; c, g: 100LS0SF; d, h: 60LS0SF

3.5.2. Rietveld phase quantification analysis

The Rietveld phase quantitative refinement of lithium slag geopolymer paste containing fly ash and varying percentages of silica fume is shown in Figure 11. The Rietveld refinement model intensity peaks showed that the quantitative phase analysis has considerable accuracy with weighted profile R-factor (Rwp) values and goodness of fit around 7 and 1, respectively. The lower R_{wp} value (<10) shows that the model and the observed peaks agree and correspond to a good quality fit. The crystalline mineral phases identified in lithium slag were anorthite, calcite, anhydrite, quartz, and spodumene. Anorthite and spodumene are the primary sources of aluminosilicates, whereas quartz and calcite are the silica and calcium sources in lithium slag. After geopolymerization, analcime and calcium chabazite were the primary binding mineral zeolites formed in LS-FA geopolymer, and the spodumene was dissolved entirely in pore solution, whereas the anorthite consumption in aluminosilicate dissolution was 2.89%. However, the dissolution of anorthite was increased to over double value (6.42%) in a geopolymer paste mix containing 50% lithium slag substitution by fly ash. It is worth mentioning that the secondary anhydrite in the geopolymer matrix surprisingly became 8.03% which was barely 1.46% in precursor lithium slag, as evident from Rietveld's quantitative analysis. However, the concentration of anhydrite was reduced to 0.03% upon incorporating 50% fly ash. Published literature revealed that the high-sulfate binder caused the precipitation of secondary gypsum by hydration of anhydrite, causing the abrupt loss of flow between 2 and 12 minutes attributed to false setting and interrupted the polycondensation of aluminosilicates [66]. A higher concentration of sulfates in lithium slag intervened in the hydration of aluminosilicates and increased water demand [11, 53]. The 100% fly ash geopolymer indicated the lowest percentage of amorphous phase in geopolymer paste, as shown in Figure 12-d, thus resulting in the lower porosity as evident in section 3.4. Therefore, the concentration of the amorphous phase in geopolymer paste is inversely proportionate to the degree of geopolymerization. The primary binding phases identified in LS-FA geopolymer were analcime, and calcium chabazite at 0, 50, and 100%, replacing lithium slag by fly ash were 5.31, 5.45, 26.58%, and 2.36, 13.32, 14.08%, respectively. Similarly, the literature suggests that the crystalline zeolites were formed under hydrothermal conditions in fly ash-based geopolymer [67]. The incorporation of 50% fly ash in lithium slag geopolymer increased the concentration of analcime from 2.36 to 13.32%, and the suppressed formation of anhydrite/gypsum is indicative of densified microstructure.

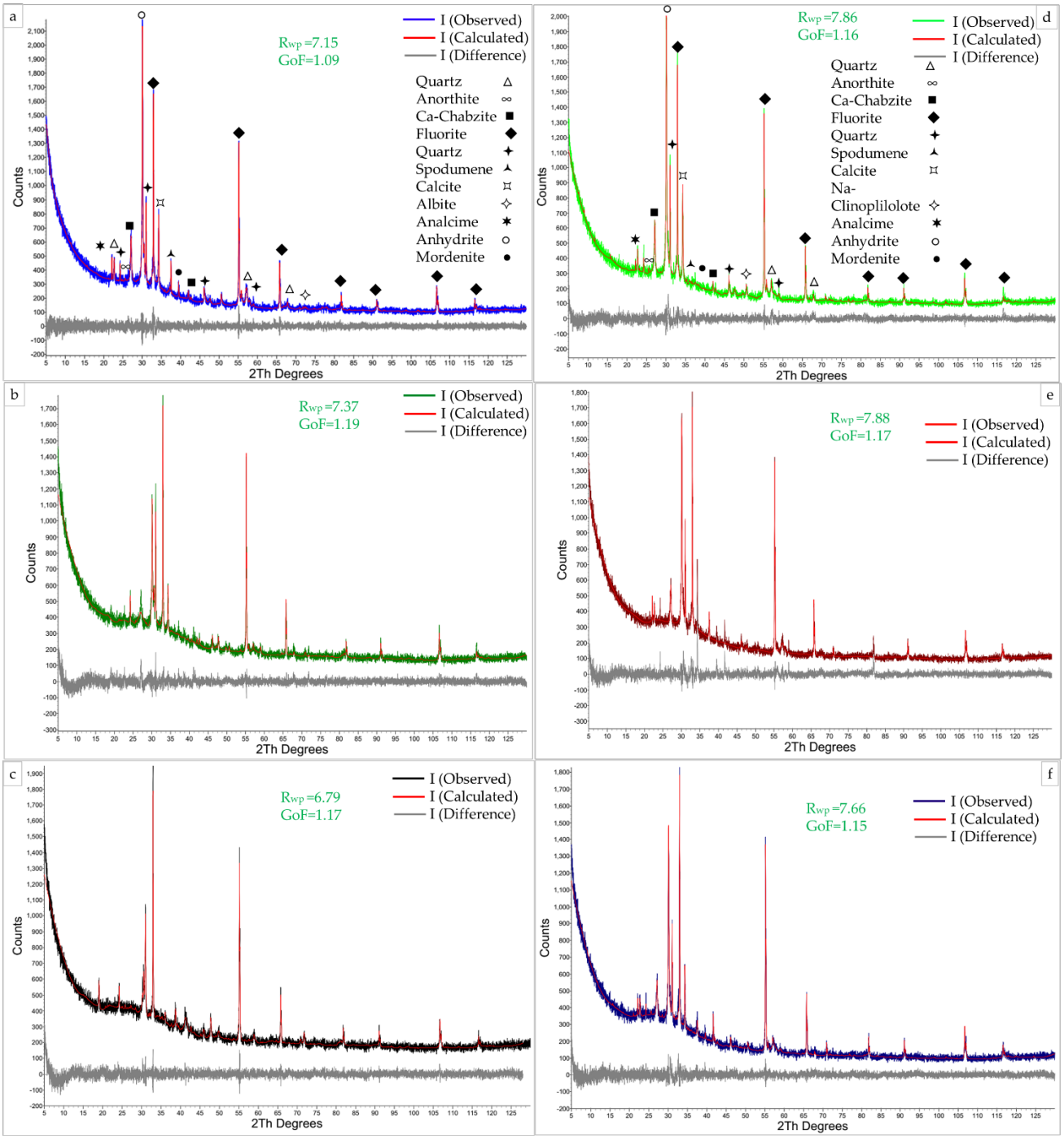

Figure 11: Quantitative phase analysis of LS-FA geopolymer paste (a: 100LS0FA, b: 50LS50FA, c: 0LS100FA) and LS-SF geopolymer d: 100LS0SF, e: 70LS30SF, f: 60LS40SF)

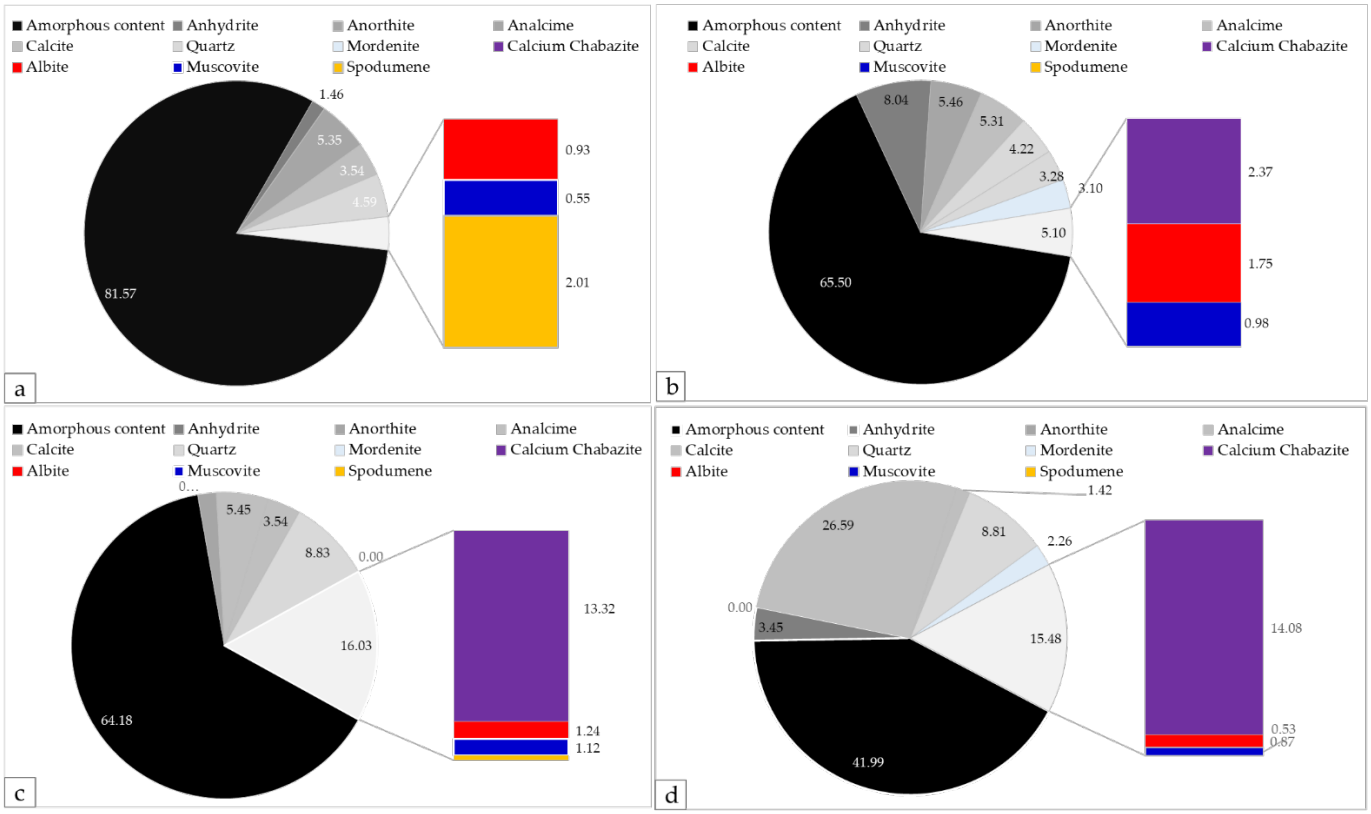

Figure 12: Crystallographic phases of LS-FA geopolymer determined by Rietveld analysis a: Calcined lithium slag, b: 100LS0FA, c: 50LS50FA, d: 0LS100FA

The phase quantification in Rietveld refinement of LS-SF geopolymer at varying proportions of silica is shown in Figure 13. At higher silica to alumina ratios, the quartz concentration increased to 10.87% for the mix containing a Si/Al ratio of 5.5. The higher concentration of added silica improved the reactivity of lithium slag geopolymer. The primary binding phases were mordenite, Na-clinoptilolite, and analcime, which increased from 6.89, 4.51, 3.50% to 7.60, 6.1, 3.80% by increasing the Si/Al ratio from 2.5 to 4.5, respectively. It is interesting to reveal that incorporations of sodium tetraborate and silica fume limit the production of gypsum/anhydrite. The sodium tetraborate added mix (100LS0SF) containing no added silica showed a percentage of anhydrite similar to that of precursor lithium slag. However, the silica addition reduced gypsum/anhydrite up to 0.76%, which was 1.04% in precursor lithium slag. It can be concluded that the presence of albite, anorthite, mordenite and quartz are the common minerals and crystal phases detected in TIMA and Rietveld quantitative analysis that primarily constitutes the aluminosilicate gel.

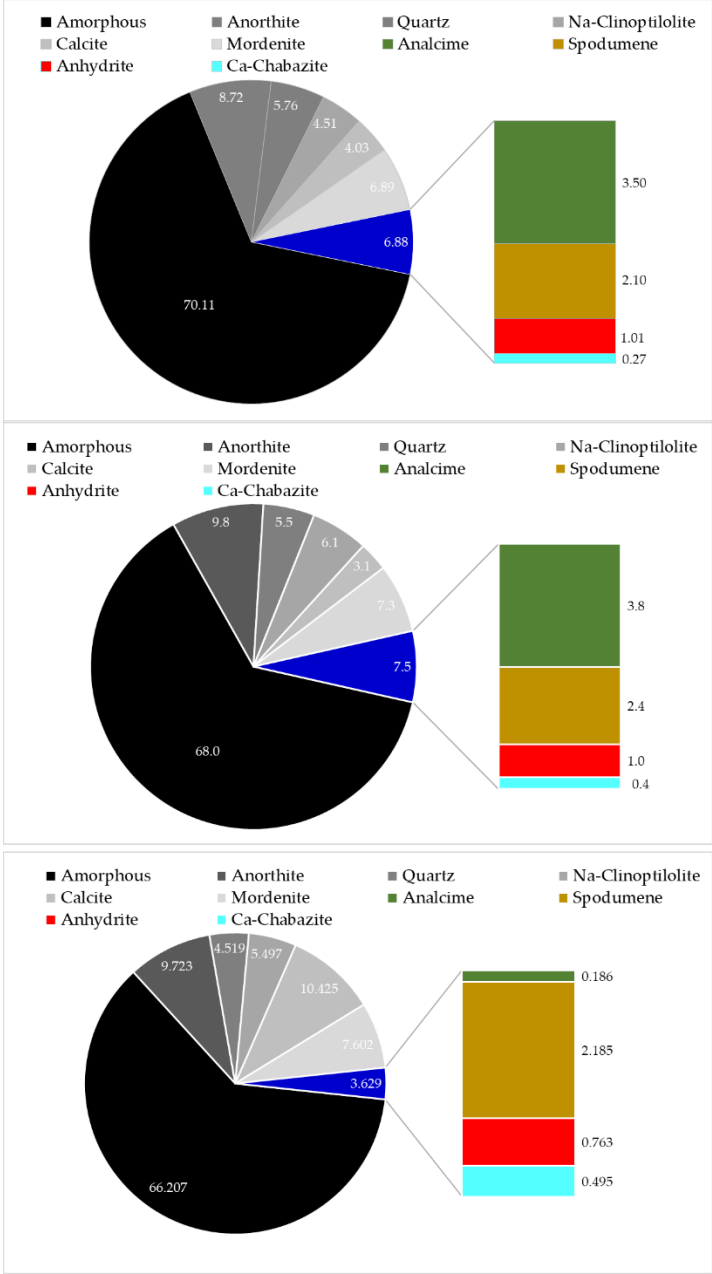

Figure 13: XRD phase quantification of geopolymer products containing varying silica content, a: 100LS0SF, b: 70LS30SF, 60LS40SF

3.5.3. Microstructural morphology of geopolymer

The SEM micrographs of lithium slag geopolymer containing fly ash and silica fume are shown in Figure 14 (a-c) and (d-f), respectively. The cumulative concentration of aluminosilicates such as anorthite, spodumene, muscovite, and albite was 7.83, rest of the aluminosilicates exists in the form of the amorphous phase, which constitutes over 80% of mass as per the results of Rietveld quantitative analysis of powdered geopolymer. The gypsum/anhydrite is evident from the concentration of SO_3^{2-} (5.62%) in XRF analysis, whereas

sodium and calcium-bearing aluminosilicates are present as albite and anorthite. The higher OH^- ion concentration dissolves Si^{4+} and Al^{3+} cations from aluminosilicates by hydrolysis of Si-O-Si and Si-O-Al bonds to form silicate hydrate ion $SiO_2(OH)^{2-}$ and aluminum hydrate tetrahedron $Al(OH)^{-4}$. The polycondensation of aluminum hydrate tetrahedron with alkali silicate hydrate constitutes C-A-S-H and N-A-S-H gel. The geopolymerization reaction occurred in two steps which are as follows [68]:

1. Dissolution of aluminosilicates and calcium sulfate

$$SiO_2 + Al_2O_3 + OH^- \rightarrow SiO_2(OH)^{2-} \; or \; SiO_2(OH)^{1-} + Al(OH)_4^-$$

$$CaSO_4 + H_2O \rightarrow Ca^{+2} + SO_4^{-2} + OH^-$$

2. Precipitation of N-A-S-H and C-A-S-H gel

$$Ca^{+2} + SiO_2(OH)_2^{2-} or \; SiO_2(OH)^{1-} + Al(OH)_4^- \rightarrow CASH \; gel$$

$$Na^+ + SiO_2(OH)_2^{2-} or \; SiO_2(OH)^{1-} + Al(OH)_4^- \rightarrow NASH \; gel$$

The systematic error of EDS detectors ranges upto 2%, as evident from the literature [69, 70]. However, it has barely affected the accuracy of EDS analysis as all the variables, including spot size, voltage, working distance, and vacuum conditions, were kept constant for all specimens. As per Rietveld's quantitative analysis, the less development of crystalline microstructure in LS-FA geopolymer paste indicates a higher concentration of amorphous phase. The EDS results on aluminosilicate gel microstructure in control lithium slag geopolymer at points A and B resulted in Ca/Si and Si/Al ratios of 0.31, 1.10, and 2.83, 2.95, respectively, depicting N-(C)-A-S-H gel. The geopolymer microstructure contains a higher sulfate concentration (SO_4^{2-}), indicating porous and cracked interfacial microstructure in Figure 14-a. The partially geopolymerized fly ash cenosphere in mix 50LS50FA at EDS point A revealed crystalline outgrowth of tubular particles rich in silica and marked by a higher Si/Al ratio of 2.34.

Moreover, the polycondensed surface of fly ash cenospheres mainly consists of mordenite-based aluminosilicate gel, as seen in section 3.5.1 (Figure 10-b). Similarly, Rodríguez et al. [71] investigated nano-silica use in fly ash geopolymer and reported the crystalline growth of silica-rich tubular particles in SEM micrographs. It is pertinent to mention that the better development of C-A-S-H gel requires a high calcium precursor, whereas N-(C)-A-S-H gel is formed in low calcium-based precursor such as in lithium slag geopolymer [72]. The SEM/EDS

analysis of LS-FA is evident that the porosity is associated with the concentration of sulfates in the geopolymer paste matrix, which causes self-desiccation. Likewise, literature [16] reported similar self-desiccation trends by adding high sulfur content in silica tailing-based cement paste, thus increasing water demand and cracking. It is worth mentioning that the absorption of sulfate in C-A-S-H gel disintegrates it and degrades the strength development of lithium slag geopolymer [16, 73]. The higher dissolution of sulfates in pore solution caused a false setting of lithium slag geopolymer paste. However, the set retardation was achieved by suppressing sulfate dissolution in pore solution upon incorporating fly ash and silica fume in geopolymer pastes. EDS analysis also revealed that the diminished EDS spectra of sulfate in the mixes 50LS50FA and 60LS40SF (Figure 14-b, e) hindered the formation of sulfates upon replacement of fly ash and silica fume. Recently published literature on lithium slag geopolymer also evidenced the flash setting being attributed to higher sulfate content [19, 29].

The microstructure of heat cured control lithium slag geopolymer containing sodium tetraborate is shown in Figure 14-d, representing the microstructure of tectosilicate zeolite. As evident in Rietveld's analysis, the added sodium tetraborate was not precipitated as a new mineral component in geopolymer paste. However, its presence in pore solution increased the dissolution rate of aluminosilicates. Similarly, Wang et al. [19] reported that sodium tetraborate did not precipitate as a phase. Instead, it remained either isolated or bounded to geopolymer matrix gel. Also, the calcium concentration was reduced, and aluminum increased by adding borax to lithium slag suspension. It is pertinent to mention that silica addition at Si/Al ratio of 5 in LS-SF geopolymer mix reduced dissolution of aluminosilicates at heat curing conditions marked by a sudden decrease in Ca/Si and Si/Al ratios (Figure 14-e). However, the same geopolymer paste mix at ambient curing conditions revealed the tightly-packed microstructure and higher silica content evident from Si/Al (5.72) at EDS area B (Figure 14-f). It is imperative from the microstructural analysis that the addition of sodium tetraborate increased the dissolution of aluminosilicate. The heat curing of LS-SF geopolymer has a deleterious effect on its microstructure that might have caused abrupt heat evolution attributed to the reactivity of silica fume. That heat evolution hindered the rate of geopolymerization for the dissolution of aluminosilicates marked by lower Ca/Si, and Si/Al ratios and subsequently caused porous microstructure attributed to thermal shrinkage. A similar phenomenon of self-desiccation of geopolymer paste matrix at the interface of quartz

particles occurred, which may contribute to the autogenous shrinkage. However, a detailed calorimetric analysis is suggested for understanding its reaction kinetics. Hence, heat curing is not recommended for silica fume added lithium slag geopolymer containing sodium tetraborate as a retarder.

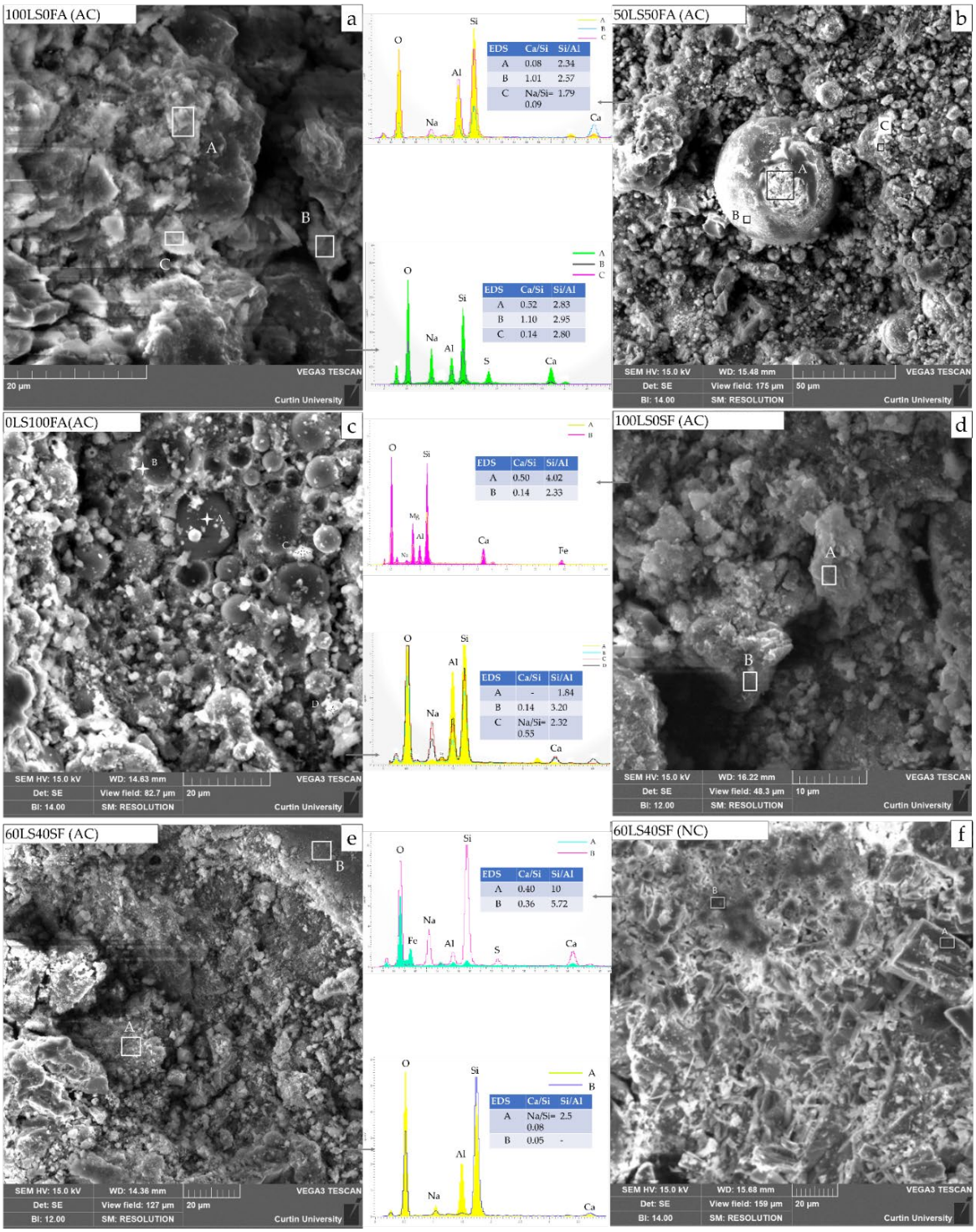

Figure 14: SEM/EDS of lithium slag geopolymer containing fly ash and silica fume (Note: AC: Specimens accelerated curing at 70˚C for 24 hours followed by ambient curing at 25˚C

and 90% relative humidity, NC: Normal curing at ambient temperature (25˚C) and humidity conditions (R.H=90%)

The SEM micrographs of a geopolymer mix in Figure 15 containing 50% fly ash and 50% lithium slag show the microstructure's amorphous and angular-edge crystalline growth. The crystalline microstructure shows the brighter microstructure in the BSE micrograph, indicating the long-chained aluminosilicates with a Si/Al ratio of 3.66 (EDS A), whereas the amorphous microstructure contains polycondensation of fly ash cenospheres and lithium slag mineral constituents. The binding phase adhering the particle of lithium slag at EDS point C appeared to be primarily composed of mordenite phase as evident from EDS spectra in TIMA analysis (Figure 10 b, f). Hence, the incorporation of 50% fly ash with lithium slag densified the microstructure of lithium slag geopolymer paste by co-precipitation of amorphous N-(C)-A-S-H gel.

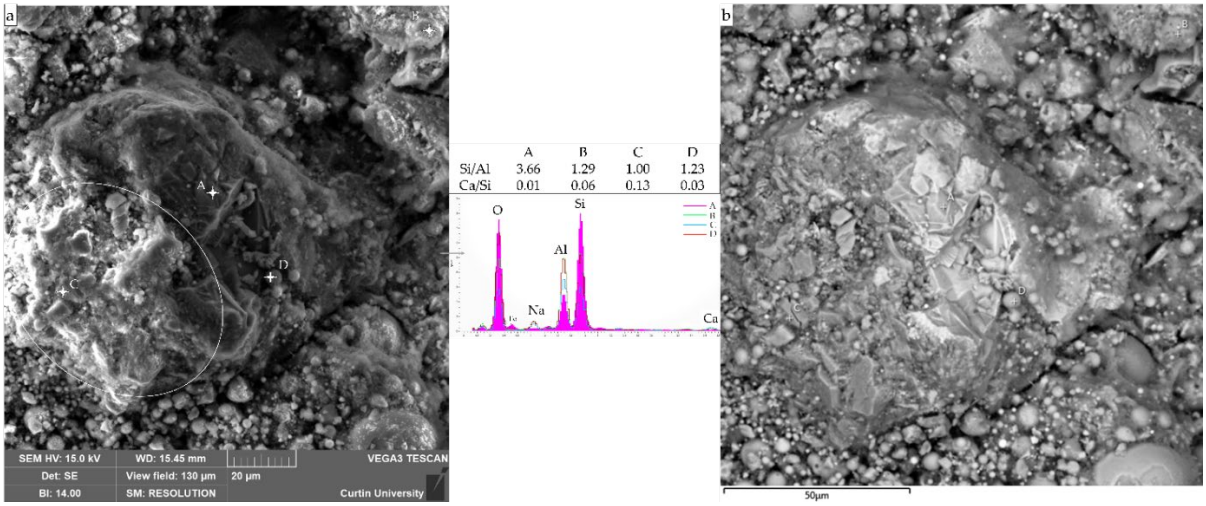

Figure 15: Microstructural development of LS-FA geopolymer (50LS50FA) a) SE micrograph b) BSE micrograph

3.6. Compressive Strength of LS-FA geopolymer

The compressive strength of fly ash added lithium slag geopolymer at heat curing conditions (70˚C for 24 hours) is shown in Figure 16. The results indicated that the compressive strength of lithium slag geopolymer improved upon the incorporation of fly ash. The percentage increase in compressive strength between incremental substitution of fly ash by 25, 50, 75, and 100% was 73.59, 41.14, 28.91, and 22.90%, respectively. The higher compressive strength of fly ash incorporated mixes is due to the densified microstructure attributed to the dissolution of aluminosilicates and formation of N-(C)-A-S-H gel, whereas the SO_4^{2-} induces porosity in C-

A-S-H gel in the geopolymer mixes with higher lithium slag proportions, consequently causing lower compressive strength. The formation of sulphatic components in high lithium slag geopolymer mixes has caused higher porosity and cracking in the geopolymer matrix. The evidence of higher sulfate content in the geopolymer paste matrix can be found in both SEM-EDS and XRD-Rietveld quantitative analysis in sections 3.5.1 and 3.5.2, respectively. The improved and densified microstructure of LS-FA geopolymer was revealed due to increased incorporation of fly ash in geopolymer matrix in SEM micrograph (Figure 14-b) alongside the lower EDS peak intensity of sulfate, depicting the suppressed formation of sulfates during geopolymerization. Moreover, the formation of mordenite phase upon fly ash incorporation contributed toward strength development of LS-FA geopolymer which appeared to fill the voids, gaps and cracks in the geopolymer microstructure as evident in section 3.5.1 (Figure 10 b, f).

Moreover, the formation of sulfates can be linked with the quantification of porosity of the geopolymer paste matrix. The reduced appearance of sulfates in alkali activation reduced 34% of voids in the hardened 50LS50FA mix. Hence, the dissolution and polycondensation reaction of alumino-silicates into geopolymer hydrates is being interrupted by recrystallization of polymorphs of gypsum owing to the presence of higher sulfate content in lithium slag.

Published literature has suggested that the dissolution of aluminosilicates in low calcium precursors such as fly ash, metakaolin, blast furnace slag, and lithium slag requires higher alkalinity than that of calcareous precursor [10, 39, 74]. Liu et al. [10] reported the lower compressive strength of lithium slag geopolymer due to the generation of microcracks. Krizan and Zivanovic [39] investigated the effect of modular ratios on early hydration of alkali-activated slag cement and reported a higher degree of dissolution of aluminosilicate at modular ratios of 1.2 and 1.5 while using sodium metasilicate as an alkaline activator. Li, Sun and Li [74] reviewed the alkali-activated slag and metakaolin binder systems and concluded that the flaky and angular microstructural morphology of blast furnace slag and metakaolin attributes the higher water demand, thus the higher drying shrinkage in geopolymer concrete. The angular microstructural morphology of ground granulated blast furnace slag can be related to the lithium slag. The angularity of lithium slag particles may have also contributed to the higher affinity of water in the geopolymer paste. Conclusively, the geopolymerization

of lithium slag geopolymer has been interrupted by higher SO_4^{-2} ions in pore solution, thus the concentration of which can be suppressed by the replacement of fly ash in lithium slag geopolymer.

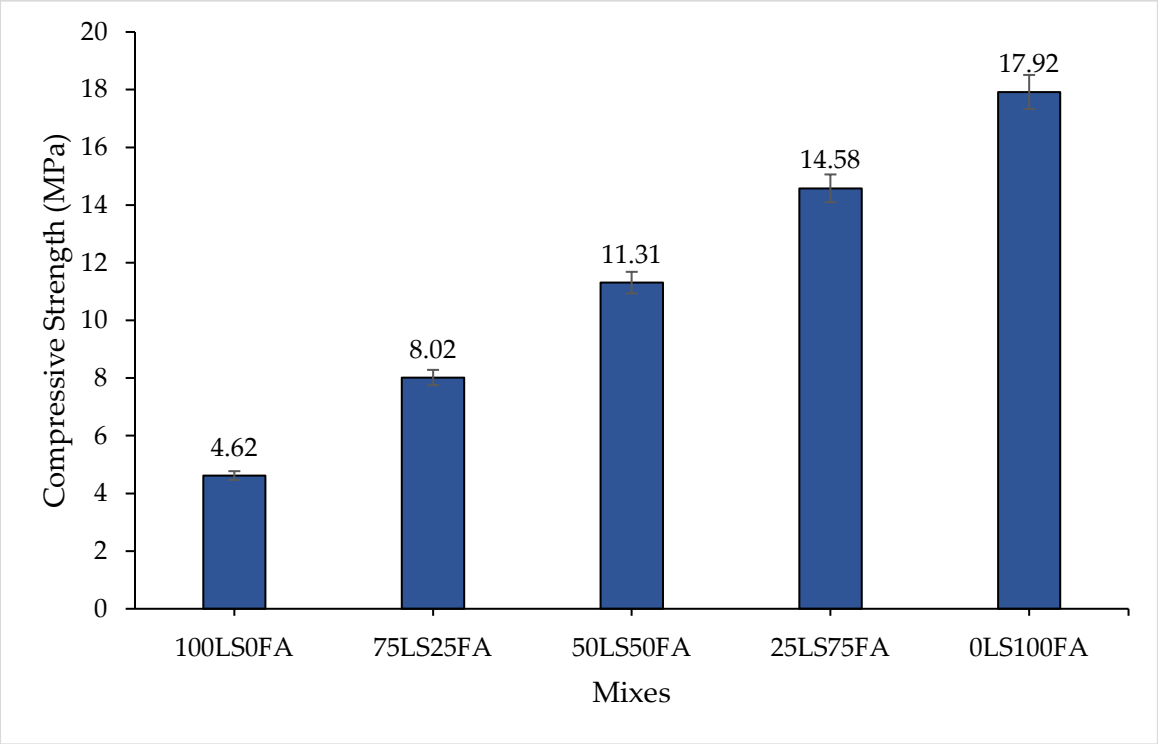

Figure 16: Compressive Strength of accelerated cured LS-FA geopolymer mixes at accelerated curing

3.7. Compressive strength of silica-containing lithium slag geopolymer

The compressive strength of ambient cured and heat cured lithium slag geopolymer paste mixes with varying Si/Al ratios are shown in Figure 17. The compressive strength of lithium slag geopolymer paste with Si/Al ratios of 2.5, 3.5, 4.5, 5.5 was 10.75, 13.17, 20.63, 21.59 MPa, respectively. The increase in compressive strength upon increasing silica content compared to control geopolymer paste was observed with the percentage increase of 22.51, 91.90, and 100.83% at Si/Al ratios of 3.5, 4.5, and 5.5, respectively. The highest percentage of compressive strength development was recorded as 69.39% between Si/Al ratios of 3.5 and 4.5 at ambient curing conditions. However, the maximum compressive strength of geopolymer paste was recorded at a Si/Al ratio of 5.5. Hence, the higher silica concentration in geopolymer mixes induced higher compressive strength.

The percentage difference between ambient and heat cured lithium slag geopolymer at Si/Al ratios of 2.5, 3.5, 4.5, and 5.5 was +86.79, -2.12, -28.97, and -22.33%, respectively. It is worth mentioning that the geopolymer paste with a Si/Al ratio of 2.5 indicated a higher compressive strength in accelerated curing than ambient curing conditions, unlike all other silica fume-added mixes. The accelerated cured control lithium slag geopolymer paste increased the compressive strength by 86.79% more than the ambient cured. Contrarily, the accelerated cured lithium slag geopolymer containing silica fume resulted in lower compressive strength. Which was due to the formation of N-(C)-A-S-H gel attributing densified microstructure to control geopolymer paste and induced cracking in silica-rich geopolymer matrix attributed to retarded formation of N-(C)-A-S-H gel as evident from EDS quantitative phase analysis (section 3.5.1). Therefore, the high temperature has a deleterious effect on the compressive strength of silica-added lithium slag geopolymer paste. It is worth mentioning that the oxide ratio of silicon to sodium (SiO_2/NaO_2) plays a vital role in the strength development of lithium slag geopolymers. A published study on sodium tetraborate added lithium slag geopolymer reported better compressive strength results at a SiO_2/NaO_2 ratio of 1, whereas the fluctuation of the stated modular ratio gets detrimental for N-(C)-A-S-H gel formation [19].

Although the lithium slag geopolymer is not extensively investigated, there are a limited number of studies in the literature on the incorporation of lithium slag as a cement replacement in concrete to cope with the waste disposal lithium slag as the reduced cement usage. However, it has the intrinsic chemical defect of higher sulfate content formed during the leaching of spodumene [8, 75-77]. The high sulfate content attributes false setting in the binder by recrystallizing gypsum into other polymorphs such as anhydrite and hemihydrate, consequently inducing hydrophilic behavior in geopolymer paste. Lithium slag has been used as a rapid hardening source in sulpho-aluminate cement due to a high concentration of reactive alumino-silicates [78]. Additionally, the potential reactivity of lithium slag suggests that its 10% substitution with silica fume in concrete produced the improved microstructure at 28 days and onward [8].

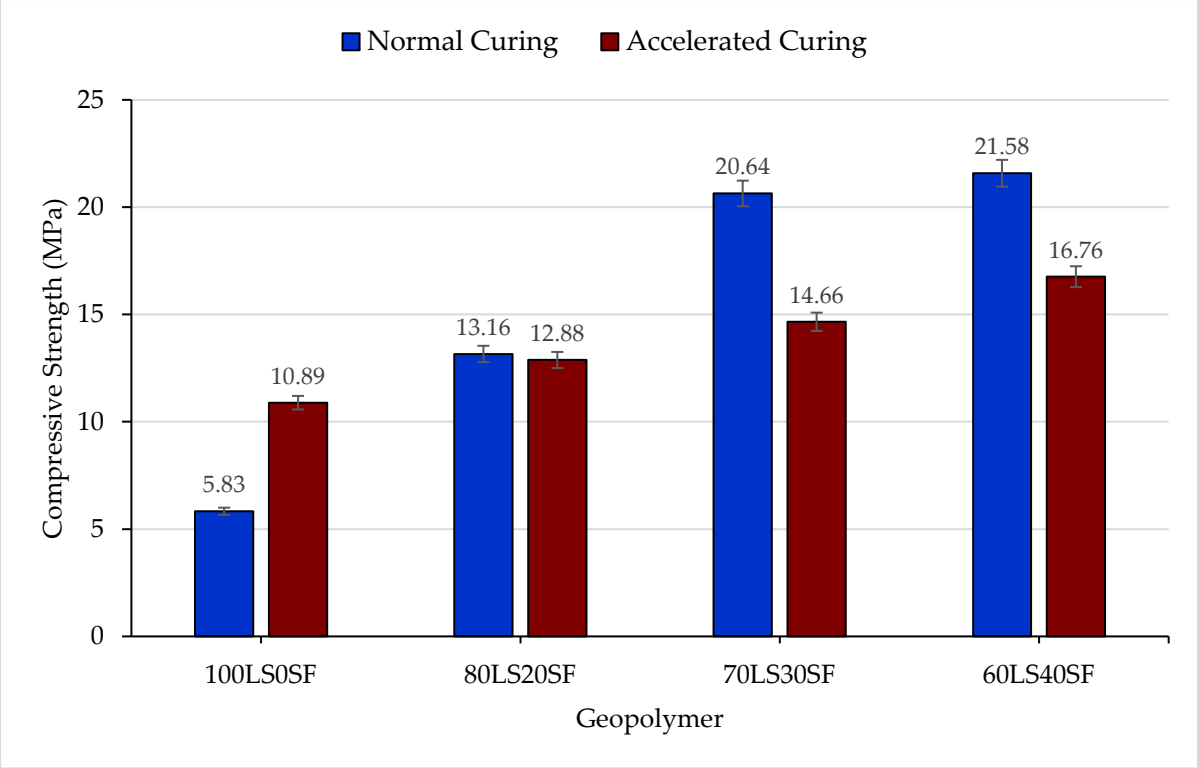

Figure 17: Compressive strength of accelerated cured lithium slag geopolymer paste at varying Si/Al ratios

4. Conclusions

Lithium slag is a lithium refinery waste chemically compatible with fly ash and silica fume to produce geopolymer binder, which provides a sustainable solution for the waste disposal of lithium slag. Its use as a geopolymer precursor along with fly ash and silica fume as chemical modifiers can provide a sustainable alternative for waste disposal and open venues for further research on its chemical optimization. The microstructural characterization of alkali aluminosilicate gel presented the main binding phases that appeared to influence the compressive strength and setting behavior of geopolymer paste. The detailed conclusions based on the experimental results are as follows:

1. The characterization of lithium slag revealed that it possesses well-distributed micro and nano-sized particles. The amorphous phase increased upon its calcination at 700˚C, which induced reactivity, whereas a higher concentration of sulfates in prismatic particles is also evident in SEM and XRF analysis. The higher sulfate concentration results in the inherent chemical shortcomings for its use as a binder.
2. Lithium slag geopolymer experienced a false setting due to the higher dissolution of sulfates $(SO_4)^{-2}$ in pore solution. The setting was retarded by the incorporation of fly ash in geopolymer, and setting time was generally increased by incremental Si/Al ratios in borax-added lithium slag geopolymer. In both types of mixes, the set retardation was carried out by suppressing sulfate dissolution in pore solution upon incorporating fly ash and silica fume, which is evident in TIMA and microstructural analysis.
3. The higher dissolution of sulfate content in the geopolymer paste matrix induced the cracking and disintegration in N-(C)-A-S-H gel. The incorporation of fly ash and increasing Si/Al ratios decreased the dissolution of sulfate content, as evident from the microstructural investigations.
4. The incorporation of fly ash in lithium slag geopolymer paste reduced its cracking by decreasing porosity. The surface pore area of geopolymer paste reduced from 7.29 to 4.76% upon 50% replacement of lithium slag by fly ash. However, the SEM/EDS analysis revealed that the porosity of geopolymer paste is associated with the concentration of sulfates.

5. The main crystallographic zeolite-based binding phases quantified in a microstructural analysis of LS-FA geopolymer were calcium chabazite, analcime, mordenite, albite, and anorthite, whereas mordenite, sodium clinoptilolite, albite, anorthite, and analcime were the zeolite-binding phases in LS-SF geopolymer.
6. The Rietveld quantitative analysis of geopolymer paste identified and quantified the zeolite-based alumino-silicate crystals marked by good quality fit. The concentration of the amorphous phase in geopolymer paste does not correspond with the compressive strength development of geopolymer pastes. Whereas, TIMA revealed the mineralogy of the aluminosilicate gel with strong visual representation. Mordenite was observed as a main binding phase, gelling the microstructure of lithium slag geopolymer. Therefore, Rietveld and TIMA analysis could be used to characterize alkali-aluminosilicate gel in geopolymer paste.
7. Sodium tetraborate added lithium slag geopolymer resulted in higher compressive strength at heat curing. However, after incorporating silica fume, the heat curing yielded lower compressive strength than that of ambient cured specimens. At the same time, the strength development increased upon the replacements of fly ash in lithium slag geopolymer at heat curing conditions. To improve strength, factors such as alkaline activator content and molarity of NaOH will be varied to evaluate the physicomechanical properties of geopolymer. Moreover, a detailed calorimetric analysis is suggested for understanding the reaction kinetics.

Acknowledgment

The authors acknowledge to Australian Research Council (ARC) for providing financial support in this research in the form of Discovery Project grant DP200102784. The authors also acknowledge the use of the state-of-the-art Tescan Integrated Mineral Analyzer (TIMA), Scanning Electron Microscope (Tescan VEGA), and X-ray Diffractometer (D8 Discover) at John De Laeter Centre at Curtin University, Australia.

References:

[1] L. Talens Peiró, G. Villalba Méndez, R.U. Ayres, Lithium: sources, production, uses, and recovery outlook, Jom 65(8) (2013) 986-996.
[2] A. Miatto, B.K. Reck, J. West, T.E. Graedel, The rise and fall of American lithium, Resources, Conservation and Recycling 162 (2020) 105034.
[3] A. Alessia, B. Alessandro, V.-G. Maria, V.-A. Carlos, B. Francesca, Challenges for sustainable lithium supply: a critical review, Journal of Cleaner Production 300 (2021) 126954.
[4] Q. Yan, X. Li, Z. Wang, X. Wu, J. Wang, H. Guo, Q. Hu, W. Peng, Extraction of lithium from lepidolite by sulfation roasting and water leaching, International Journal of Mineral Processing 110 (2012) 1-5.
[5] B.W. Jaskula, Lithium, in: U.S.G. Survey (Ed.) 2019.
[6] J.-M. Tarascon, M. Armand, Issues and challenges facing rechargeable lithium batteries, Materials for sustainable energy: a collection of peer-reviewed research and review articles from Nature Publishing Group (2011) 171-179.
[7] B.W. Jaskula, Lithium, in: U.S.G. Survey (Ed.) 2021.
[8] Z.-h. He, S.-g. Du, D. Chen, Microstructure of ultra high performance concrete containing lithium slag, Journal of hazardous materials 353 (2018) 35-43.
[9] D. Chen, X. Hu, L. Shi, Q. Cui, H. Wang, H. Yao, Synthesis and characterization of zeolite X from lithium slag, Applied Clay Science 59 (2012) 148-151.
[10] Z. Liu, Wang, Jixiang, Jiang, Qikan, Cheng, Guodong, Li, Li, Kang, Yixing, Wang, Dongmin, A green route to sustainable alkali-activated materials by heat and chemical activation of lithium slag, Journal of Cleaner Production 225 (2019) 1184-1193.
[11] Y. He, Q. Zhang, Q. Chen, J. Bian, C. Qi, Q. Kang, Y. Feng, Mechanical and environmental characteristics of cemented paste backfill containing lithium slag-blended binder, Construction and Building Materials 271 (2021) 121567.
[12] S.F.A. Shah, B. Chen, M.R. Ahmad, M.A. Haque, Development of Cleaner One-part geopolymer from lithium slag, Journal of Cleaner Production 291 (2021) 125241.
[13] L.I. Barbosa, G. Valente, R.P. Orosco, J.A. Gonzalez, Lithium extraction from β-spodumene through chlorination with chlorine gas, Minerals Engineering 56 (2014) 29-34.
[14] P.K. Choubey, M.-s. Kim, R.R. Srivastava, J.-c. Lee, J.-Y. Lee, Advance review on the exploitation of the prominent energy-storage element: Lithium. Part I: From mineral and brine resources, Minerals Engineering 89 (2016) 119-137.
[15] O. Peltosaari, P. Tanskanen, E.-P. Heikkinen, T. Fabritius, $\alpha \rightarrow \gamma \rightarrow$ β-phase transformation of spodumene with hybrid microwave and conventional furnaces, Minerals Engineering 82 (2015) 54-60.
[16] W. Li, M. Fall, Sulphate effect on the early age strength and self-desiccation of cemented paste backfill, Construction and Building Materials 106 (2016) 296-304.
[17] M. Collepardi, A state-of-the-art review on delayed ettringite attack on concrete, Cement and concrete Composites 25(4-5) (2003) 401-407.
[18] Y. Qiu, D. Wu, L. Yan, Y. Zhou, Recycling of spodumene slag: preparation of green polymer composites, RSC advances 6(43) (2016) 36942-36953.
[19] J. Wang, L. Han, Z. Liu, D. Wang, Setting controlling of lithium slag-based geopolymer by activator and sodium tetraborate as a retarder and its effects on mortar properties, Cement and Concrete Composites 110 (2020) 103598.

[20] J. Bensted, I.C. Callaghan, A. Lepre, Comparative study of the efficiency of various borate compounds as set-retarders of class G oilwell cement, Cement and concrete research 21(4) (1991) 663-668.
[21] M. Zajac, J. Skocek, F. Bullerjahn, M.B. Haha, Effect of retarders on the early hydration of calcium-sulpho-aluminate (CSA) type cements, Cement and Concrete Research 84 (2016) 62-75.
[22] C.L. Nicholson, B.J. Murray, R.A. Fletcher, D. Brew, K.J. Mackenzie, M. Schmücker, Novel geopolymer materials containing borate structural units, World Congress Geopolymer, 2005, pp. 31-33.
[23] F.U.A. Shaikh, Mechanical properties of recycled aggregate concrete containing ternary blended cementitious materials, International Journal of Sustainable Built Environment 6(2) (2017) 536-543.
[24] G. Mie, Annalen der Physik. 1908, B 25 377-445.
[25] R. Kleeberg, T. Monecke, S. Hillier, Preferred orientation of mineral grains in sample mounts for quantitative XRD measurements: How random are powder samples?, Clays and clay minerals 56(4) (2008) 404-415.
[26] F.S. Usman Javed, Prabir Sarker, Microstructural investigation of thermo-mechanically processed lithium slag for geopolymer precursor using various characterization techniques, Construction and Building Materials (2022).
[27] J. Meng, L. Xu, L. Luo, K. Shu, Effects of grinding media on the flotation behavior of spodumene in mixed anionic/cationic collectors system, Colloids and Surfaces A: Physicochemical and Engineering Aspects 627 (2021) 127213.
[28] N.K. Salakjani, P. Singh, A.N. Nikoloski, Acid roasting of spodumene: Microwave vs. conventional heating, Minerals Engineering 138 (2019) 161-167.
[29] U. Javed, F.U.A. Shaikh, P.K. Sarker, Microstructural investigation of thermo-mechanically processed lithium slag for geopolymer precursor using various characterization techniques, Construction and Building Materials 342 (2022) 127952.
[30] Q. Wan, F. Rao, S. Song, R.E. García, R.M. Estrella, C.L. Patino, Y. Zhang, Geopolymerization reaction, microstructure and simulation of metakaolin-based geopolymers at extended Si/Al ratios, Cement and Concrete Composites 79 (2017) 45-52.
[31] P. Duxson, A. Fernández-Jiménez, J.L. Provis, G.C. Lukey, A. Palomo, J.S. van Deventer, Geopolymer technology: the current state of the art, Journal of materials science 42(9) (2007) 2917-2933.
[32] C. Leiva, Y. Luna-Galiano, C. Arenas, B. Alonso-Fariñas, C. Fernández-Pereira, A porous geopolymer based on aluminum-waste with acoustic properties, Waste Management 95 (2019) 504-512.
[33] H. Assaedi, T. Alomayri, C.R. Kaze, B.B. Jindal, S. Subaer, F. Shaikh, S. Alraddadi, Characterization and properties of geopolymer nanocomposites with different contents of nano-CaCO3, Construction and Building Materials 252 (2020) 119137.
[34] D. Bondar, C. Lynsdale, N. Milestone, N. Hassani, A. Ramezanianpour, Effect of heat treatment on reactivity-strength of alkali-activated natural pozzolans, Construction and Building Materials 25(10) (2011) 4065-4071.
[35] R.P. Williams, A. Van Riessen, Determination of the reactive component of fly ashes for geopolymer production using XRF and XRD, Fuel 89(12) (2010) 3683-3692.
[36] P. Rovnaník, P. Rovnanikova, M. Vyšvařil, S. Grzeszczyk, E. Janowska-Renkas, Rheological properties and microstructure of binary waste red brick powder/metakaolin geopolymer, Construction and Building Materials 188 (2018) 924-933.

[37] H. Abdel-Gawwad, K.A. Khalil, Application of thermal treatment on cement kiln dust and feldspar to create one-part geopolymer cement, Construction and Building Materials 187 (2018) 231-237.
[38] F. Uddin Ahmed Shaikh, S. Haque, J. Sanjayan, Behavior of fly ash geopolymer as fire resistant coating for timber, Journal of Sustainable Cement-Based Materials 8(5) (2019) 259-274.
[39] D. Krizan, B. Zivanovic, Effects of dosage and modulus of water glass on early hydration of alkali–slag cements, Cement and concrete research 32(8) (2002) 1181-1188.
[40] S. Oyebisi, A. Ede, O.M. Ofuyatan, J. Oluwafemi, F. Olutoge, Modeling of hydrogen potential and compressive strength of geopolymer concrete, International Journal of Civil Engineering and Technology (IJCIET) 9(7) (2018) 671-679.
[41] H. Chen, C. Qian, H. Huang, Self-healing cementitious materials based on bacteria and nutrients immobilized respectively, Construction and Building Materials 126 (2016) 297-303.
[42] A.S. De Vargas, D.C. Dal Molin, A.C. Vilela, F.J. Da Silva, B. Pavao, H. Veit, The effects of Na2O/SiO2 molar ratio, curing temperature and age on compressive strength, morphology and microstructure of alkali-activated fly ash-based geopolymers, Cement and concrete composites 33(6) (2011) 653-660.
[43] W. Franus, R. Panek, M. Wdowin, SEM investigation of microstructures in hydration products of portland cement, 2nd international multidisciplinary microscopy and microanalysis congress, Springer, 2015, pp. 105-112.
[44] Y. Gao, Z. Li, J. Zhang, Q. Zhang, Y. Wang, Synergistic use of industrial solid wastes to prepare belite-rich sulphoaluminate cement and its feasibility use in repairing materials, Construction and Building Materials 264 (2020) 120201.
[45] S. Hanjitsuwan, B. Injorhor, T. Phoo-ngernkham, N. Damrongwiriyanupap, L.-Y. Li, P. Sukontasukkul, P. Chindaprasirt, Drying shrinkage, strength and microstructure of alkali-activated high-calcium fly ash using FGD-gypsum and dolomite as expansive additive, Cement and Concrete Composites 114 (2020) 103760.
[46] N. Lee, J.G. Jang, H.-K. Lee, Shrinkage characteristics of alkali-activated fly ash/slag paste and mortar at early ages, Cement and Concrete Composites 53 (2014) 239-248.
[47] G.S. Ryu, Y.B. Lee, K.T. Koh, Y.S. Chung, The mechanical properties of fly ash-based geopolymer concrete with alkaline activators, Construction and building materials 47 (2013) 409-418.
[48] X. Zhao, C. Liu, L. Zuo, L. Wang, Q. Zhu, M. Wang, Investigation into the effect of calcium on the existence form of geopolymerized gel product of fly ash based geopolymers, Cement and Concrete Composites 103 (2019) 279-292.
[49] T. Westphal, T. Füllmann, H. Pöllmann, Rietveld quantification of amorphous portions with an internal standard—Mathematical consequences of the experimental approach, Powder Diffraction 24(3) (2009) 239-243.
[50] A. ASTM, C191-13 Standard Test Methods for Time of Setting of Hydraulic Cement by Vicat Needle, ASTM International: West Conshohocken, PA, USA (2013).
[51] A. C109/C109M, Standard Test Method for Compressive Strength of Hydraulic Cement Mortars (Using 2-in. or [50 mm] Cube Specimens)1, 2022.
[52] H.F. Taylor, Cement chemistry, Thomas Telford London1997.
[53] A. Ghirian, M. Fall, Coupled behavior of cemented paste backfill at early ages, Geotechnical and Geological Engineering 33(5) (2015) 1141-1166.
[54] H. Ye, A. Radlińska, Shrinkage mitigation strategies in alkali-activated slag, Cement and Concrete Research 101 (2017) 131-143.

[55] F. Matalkah, T. Salem, M. Shaafaey, P. Soroushian, Drying shrinkage of alkali activated binders cured at room temperature, Construction and Building Materials 201 (2019) 563-570.
[56] P. Chindaprasirt, P. De Silva, K. Sagoe-Crentsil, S. Hanjitsuwan, Effect of SiO2 and Al2O3 on the setting and hardening of high calcium fly ash-based geopolymer systems, Journal of Materials Science 47(12) (2012) 4876-4883.
[57] M. Nuruzzaman, J.C. Kuri, P.K. Sarker, Strength, permeability and microstructure of self-compacting concrete with the dual use of ferronickel slag as fine aggregate and supplementary binder, Construction and Building Materials 318 (2022) 125927.
[58] S.A. Khawaja, U. Javed, T. Zafar, M. Riaz, M.S. Zafar, M.K. Khan, Eco-friendly incorporation of sugarcane bagasse ash as partial replacement of sand in foam concrete, Cleaner Engineering and Technology 4 (2021) 100164.
[59] S. Adjei, S. Elkatatny, K. Ayranci, Effect of Elevated Temperature on the Microstructure of Metakaolin-Based Geopolymer, ACS omega 7(12) (2022) 10268-10276.
[60] J. Davidovits, Geopolymers: inorganic polymeric new materials, Journal of Thermal Analysis and calorimetry 37(8) (1991) 1633-1656.
[61] V. Glukhovsky, Ancient, modern and future concretes, Proceedings of the First International Conference on Alkaline Cements and Concretes, Kiev, Ukraine, 1994, pp. 1-9.
[62] J.L. Bell, P. Sarin, P.E. Driemeyer, R.P. Haggerty, P.J. Chupas, W.M. Kriven, X-ray pair distribution function analysis of a metakaolin-based, KAlSi 2 O 6· 5.5 H 2 O inorganic polymer (geopolymer), Journal of Materials Chemistry 18(48) (2008) 5974-5981.
[63] J.L. Bell, P. Sarin, J.L. Provis, R.P. Haggerty, P.E. Driemeyer, P.J. Chupas, J.S. Van Deventer, W.M. Kriven, Atomic structure of a cesium aluminosilicate geopolymer: a pair distribution function study, Chemistry of Materials 20(14) (2008) 4768-4776.
[64] C.E. White, J.L. Provis, T. Proffen, J.S. Van Deventer, The effects of temperature on the local structure of metakaolin-based geopolymer binder: A neutron pair distribution function investigation, Journal of the American Ceramic Society 93(10) (2010) 3486-3492.
[65] C.E. White, J.L. Provis, A. Llobet, T. Proffen, J.S. Van Deventer, Evolution of local structure in geopolymer gels: an in situ neutron pair distribution function analysis, Journal of the American Ceramic Society 94(10) (2011) 3532-3539.
[66] F.J. Tang, E.M. Gartner, Influence of sulphate source on Portland cement hydration, Advances in Cement Research 1(2) (1988) 67-74.
[67] N. Lee, H.R. Khalid, H.-K. Lee, Synthesis of mesoporous geopolymers containing zeolite phases by a hydrothermal treatment, Microporous and Mesoporous Materials 229 (2016) 22-30.
[68] P. Chindaprasirt, P. De Silva, K. Sagoe-Crentsil, S. Hanjitsuwan, Effect of SiO 2 and Al 2 O 3 on the setting and hardening of high calcium fly ash-based geopolymer systems, Journal of Materials Science 47(12) (2012) 4876-4883.
[69] P. Echlin, C. Fiori, J. Goldstein, D.C. Joy, D.E. Newbury, Advanced scanning electron microscopy and X-ray microanalysis, Springer Science & Business Media2013.
[70] M. Australia, My Scope, Microscopy Training. https://myscope.training/#/EDSlevel_2_29. (Accessed 28-06-2022.
[71] E.D. Rodríguez, Bernal, Susan A, Provis, John L, Paya, Jordi, Monzo, José M, Borrachero, María Victoria, Effect of nanosilica-based activators on the performance of an alkali-activated fly ash binder, Cement and Concrete Composites 35(1) (2013) 1-11.
[72] I. García-Lodeiro, A. Palomo, A. Fernández-Jiménez, D. Macphee, Compatibility studies between NASH and CASH gels. Study in the ternary diagram Na2O–CaO–Al2O3–SiO2–H2O, Cement and Concrete Research 41(9) (2011) 923-931.

[73] S. Puligilla, P. Mondal, Role of slag in microstructural development and hardening of fly ash-slag geopolymer, Cement and concrete Research 43 (2013) 70-80.
[74] C. Li, H. Sun, L. Li, A review: The comparison between alkali-activated slag (Si+ Ca) and metakaolin (Si+ Al) cements, Cement and concrete research 40(9) (2010) 1341-1349.
[75] Z.-h. He, L.-y. Li, S.-g. Du, Mechanical properties, drying shrinkage, and creep of concrete containing lithium slag, Construction and Building Materials 147 (2017) 296-304.
[76] Y. WEN, G.-j. LIU, Z.-y. QIN, K. ABULA, Y.-f. SONG, Study on the effect of lithium slag pow ders upon the chloride penetration of concrete [J], Concrete 8 (2011) 76-78.
[77] F.F. Wu, K.B. Shi, S.K. Dong, Influence of concrete with lithium-slag and steel slag by early curing conditions, Key Engineering Materials, Trans Tech Publ, 2014, pp. 52-55.
[78] H. Tan, X. Zhang, X. He, Y. Guo, X. Deng, Y. Su, J. Yang, Y. Wang, Utilization of lithium slag by wet-grinding process to improve the early strength of sulphoaluminate cement paste, Journal of Cleaner Production 205 (2018) 536-551.